ACS NANO
Cite This: ACS Nano XXXX, XXX, XXX−XXX
www.acsnano.org

ARTICLE

Targeted Brain Delivery of Rabies Virus Glycoprotein 29-Modified Deferoxamine-Loaded Nanoparticles Reverses Functional Deficits in Parkinsonian Mice

Linhao You,[†,‡,△] Jing Wang,[‡,∥,△] Tianqing Liu,[§,△] Yinlong Zhang,[‡,⊥] Xuexiang Han,[‡,∥] Ting Wang,[¶] Shanshan Guo,[‡,∥] Tianyu Dong,[†] Junchao Xu,[‡,∥] Gregory J. Anderson,[§] Qiang Liu,[#] Yan-Zhong Chang,[*,†] Xin Lou,[*,¶] and Guangjun Nie[*,‡,∥]

[†]Laboratory of Molecular Iron Metabolism, College of Life Science, Hebei Normal University, Shijiazhuang, Hebei Province 050024, China

[‡]CAS Key Laboratory for Biomedical Effects of Nanomaterials and Nanosafety, CAS Center for Excellence in Nanoscience, National Center for Nanoscience and Technology, Beijing 100190, China

[§]QIMR Berghofer Medical Research Institute, PO Royal Brisbane Hospital, Brisbane, QLD 4029, Australia

[⊥]College of Pharmaceutical Science, Jilin University, Changchun 130021, China

[∥]University of Chinese Academy of Sciences, Beijing 100049, China

[¶]Department of Radiology, The People's Liberation Army General Hospital, No. 28 Fuxing Road, Beijing 100853, China

[#]Chinese Academy of Sciences Key Laboratory of Brain Function and Disease, and School of Life Sciences, University of Science and Technology of China, Hefei 230026, China

Supporting Information

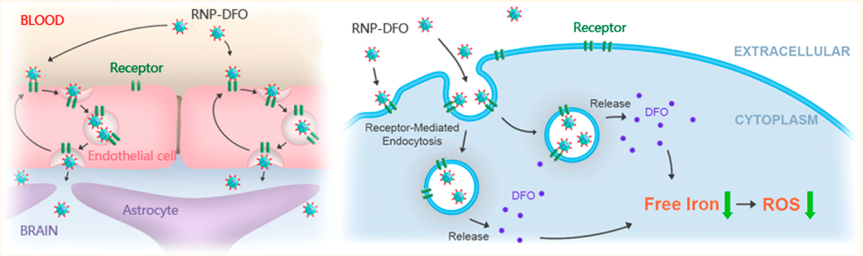

ABSTRACT: **Excess iron deposition in the brain often causes oxidative stress-related damage and necrosis of dopaminergic neurons in the substantia nigra and has been reported to be one of the major vulnerability factors in Parkinson's disease (PD). Iron chelation therapy using deferoxamine (DFO) may inhibit this nigrostriatal degeneration and prevent the progress of PD. However, DFO shows very short half-life *in vivo* and hardly penetrates the blood brain barrier (BBB). Hence, it is of great interest to develop DFO formulations for safe and efficient intracerebral drug delivery. Herein, we report a polymeric nanoparticle system modified with brain-targeting peptide rabies virus glycoprotein (RVG) 29 that can intracerebrally deliver DFO. The nanoparticle system penetrates the BBB possibly through specific receptor-mediated endocytosis triggered by the RVG29 peptide. Administration of these nanoparticles significantly decreased iron content and oxidative stress levels in the substantia nigra and striatum of PD mice and effectively reduced their dopaminergic neuron damage and as reversed their neurobehavioral deficits, without causing any overt adverse effects in the brain or other organs. This DFO-based nanoformulation holds great promise for delivery of DFO into the brain and for realizing iron chelation therapy in PD treatment.**

KEYWORDS: *blood brain barrier, deferoxamine, Parkinson's disease, rabies virus glycoprotein 29, polymeric nanoparticles*

Parkinson's disease (PD) is one of the most concerning neurodegenerative diseases that affects approximately 2% population worldwide and is characterized by degeneration of dopaminergic neurons in the substantia nigra (SN). The

Received: November 17, 2017
Accepted: March 29, 2018

DOI: 10.1021/acsnano.7b08172
ACS Nano XXXX, XXX, XXX−XXX

Scheme 1. Scheme of the Construction of RNP-DFO Nanoparticles and the Proposed Mechanism of Action[a]

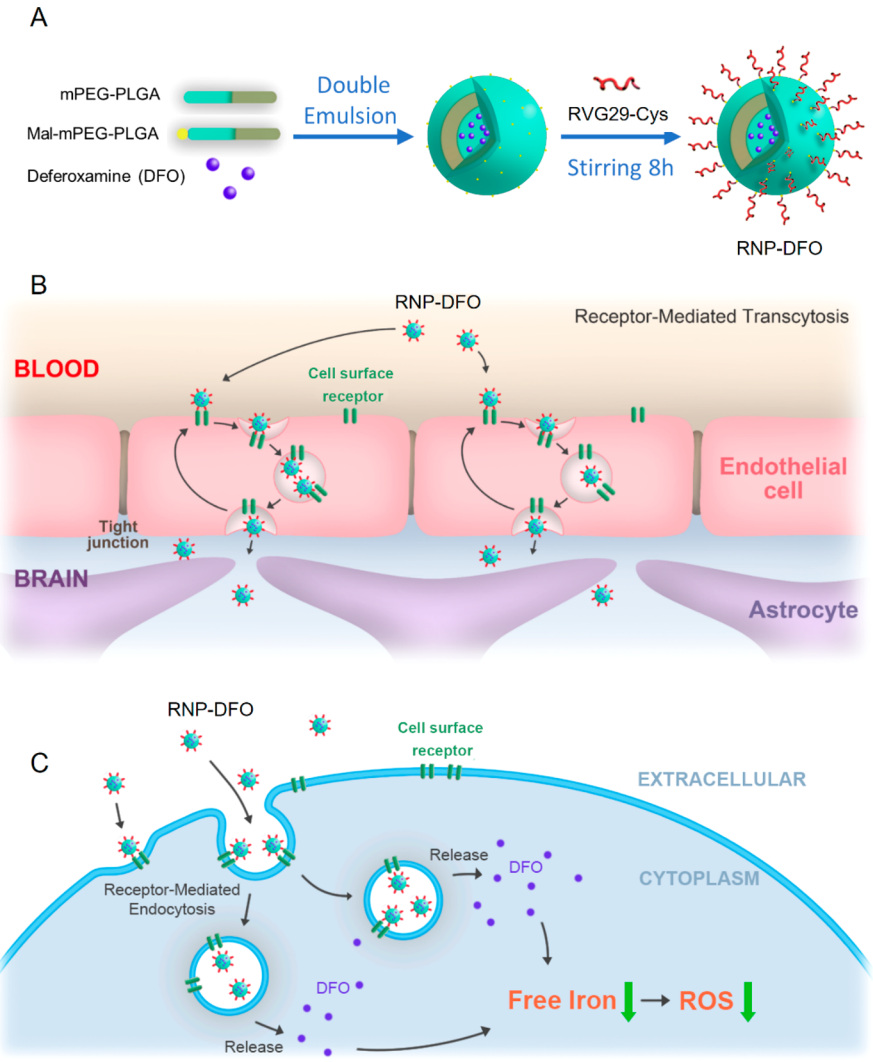

[a](A) Schematic diagram of the synthesis of RNP-DFO nanoparticle. Polymer nanoparticles were fabricated by a double emulsion method, and RVG29-Cys was linked to the nanoparticle surface *via* a maleimide−thiol coupling reaction. (B) Schematic illustration of the proposed mechanism of the penetration of RNP-DFO across the BBB. RVG29 peptide binds cell surface receptors on the brain endothelial cells that form the BBB, which further mediates the transcytosis of nanoparticles across the cell layer. (C) Proposed action of RNP-DFO in iron-loaded neuron cells. Internalization of RNP-DFO allows the released DFO to remove excess cellular iron and reduce iron-related oxidative stress.

loss of dopaminergic neurons results in motor dysfunctions along with nonmotor symptoms.[1−3] Previous *post mortem* studies often observe iron overload in Parkinsonian SN.[4] Similar results have also been reported in imaging studies such as magnetic resonance and transcranial ultrasound.[5,6] Excess iron deposition in SN is therefore thought to be a common characteristic among PD patients.[4] Iron overload is known to induce excess reactive oxygen species (ROS), which leads to oxidative stress, dysfunction of organelles, and consequently necrosis of dopaminergic neurons.[7,8] Animal studies confirmed that injection of ferric iron into SN results in progressive Parkinsonism,[9,10] and that intraperitoneal infusion with iron dextran leads to the apoptosis and necrosis of dopaminergic neurons.[11] These clues together suggest that iron overload is one of the precipitating factors leading to the degeneration of dopaminergic neurons and is closely associated with PD.

Removing the excess iron using chelators with high affinities for iron may protect dopaminergic neurons against oxidative stress and may be a promising PD treatment. Among the iron chelators that are now used clinically, deferoxamine (DFO) has been shown to be the most effective with the most favorable toxicity profile.[12,13] DFO is also one of only three iron chelation drugs approved by the U.S. Food and Drug Administration for iron overload disease, and its application in refractory anemia, such as β-thalassemia, has greatly improved the life quality and duration of patients. A few animal studies have already shown that DFO prevents dopaminergic neuronal death and inhibits nigrostriatal degeneration in PD models induced by 1-methyl-4-phenyl-1,2,3,6-tetrahydropyridine (MPTP) or 6-hydroxydopamine.[14,15] Unfortunately, DFO is not suitable for oral administration due to poor bioavailability, and it has a very short plasma half-life (20 min in humans).[16] Therapies based on DFO often require 5−7 overnight subcutaneous infusions per week to yield significant iron excretion, causing great inconvenience for the patients.[13,17,18] In addition, despite being better tolerated than other iron chelators, DFO still has serious side effects at the high doses required by such treatment, including renal and liver complications.[12,13] Moreover, the

DOI: 10.1021/acsnano.7b08172
ACS Nano XXXX, XXX, XXX−XXX

Table 1. Characterization of Nanoparticles with Different Composition[a]

formulation	size (nm)	PDI	ξ (mV)	EE (%)	LE (%)
NP	174.8 ± 1.5	0.181 ± 0.014	−27.60 ± 0.38		
RNP	175.1 ± 2.9	0.168 ± 0.008	−25.23 ± 0.29		
NP-DFO	167.2 ± 1.7	0.145 ± 0.037	−28.70 ± 0.22	45.7 ± 4.3	9.5 ± 1.1
RNP-DFO	168.8 ± 1.9	0.165 ± 0.043	−27.40 ± 0.71	45.2 ± 2.8	9.2 ± 0.9

[a]Size (diameter, nm) and polydispersity index (PDI) and ζ-potential (ξ) were determined by dynamic light scattering. Encapsulation and loading efficiencies (EE and LE, respectively) of DFO in NP-DFO and RNP-DFO were measured with a spectrophotometer. Data represent mean ± SD from six independent preparations. The dispersant of nanoparticles was triple-distilled water.

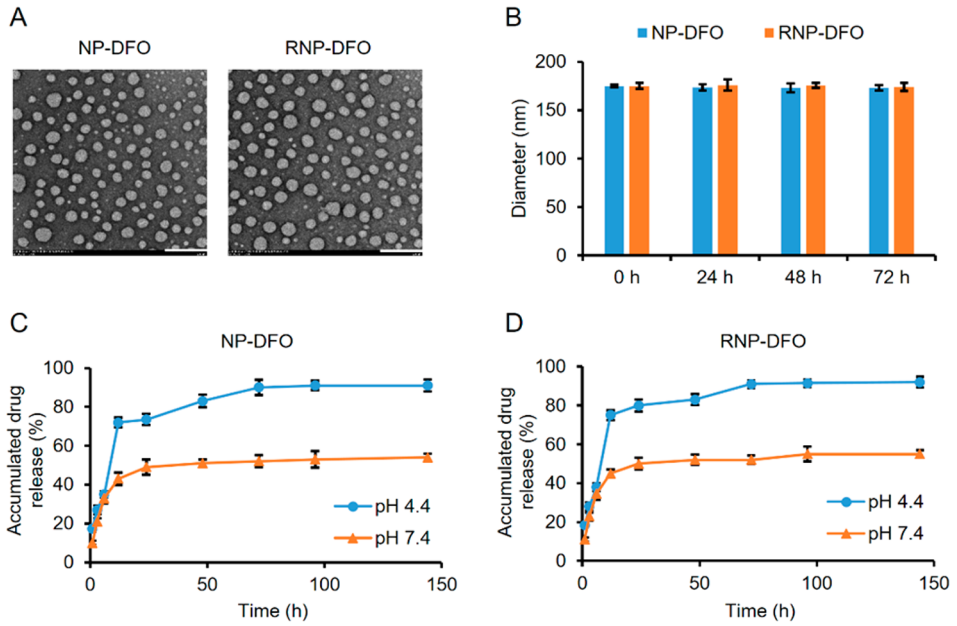

Figure 1. Characterization of DFO-loaded nanoparticles. (A) Photomicrographs of NP-DFO and RNP-DFO taken through TEM depict their smooth spherical morphology. Scale bar = 200 nm. (B) Diameter of NP-DFO and RNP-DFO before (0 h) and after being incubated in PBS (pH 7.4) for different time periods as determined by DLS. No significant size change occurred in 72 h, suggesting that the nanoparticles are stable. Data are presented as mean ± SD from three independent experiments. (C,D) Release kinetics of DFO under mimic physiological conditions from NP-DFO (C) and RNP-DFO (D) at pH 4.4 and 7.4.

hydrophilic nature of DFO leads to its poor ability in penetrating the blood brain barrier (BBB),[19] and delivering DFO drug to the brain remains a major challenge for its potential application in the treatment of PD. Therefore, developing safe and effective delivery approaches for the intracerebral delivery of DFO becomes an urgent need.

In recent years, brain-targeted nanocarriers, especially polymeric nanoparticles, emerged as a promising solution for drug delivery across the BBB. Through conjugation with specific brain-targeting ligands, such as antitransferrin receptor-1 antibodies, polymeric drug delivery systems not only enable the intracerebral delivery of otherwise BBB-impermeable therapeutic agents but also may improve their pharmacokinetic profiles.[20,21] However, the efficacy and brain specificity of the existing systems are still limited, and development of BBB-penetrating nanoparticles is of great interest. In particular, to our best knowledge, no such nanosystem has yet been developed to deliver DFO into the brain.

Rabies virus glycoprotein (RVG) is a protein that specifically binds the nicotinic acetylcholine receptor (nAchR),[22] a receptor widely located on the extracellular surface of brain microvascular endothelial cells as well as neurons. A 29 amino acid peptide derived from RVG, RVG29, has also been reported to bind nAchR and to effectively cross the BBB, possibly *via* nAchR-mediated transcytosis.[23−25] Another possible mediator suggested for the BBB penetration of RVG29 is a receptor of neurotransmitter γ-aminobutyric acid (GABA).[26] It has been demonstrated that conjugation with RVG29 enhanced the brain-related efficacy of various agents, including nucleic acids, proteins, and nanoparticles when administered systemically.[26−28] Currently, the potential of RVG29-mediated delivery of iron chelators for intracerebral applications remains unexplored.

In this study, we report an RVG29-conjugated monomethoxy-poly(ethylene glycol) (mPEG)-poly(lactic-*co*-glycolic acid) (PLGA) nanoparticle (RNP-DFO) that allows both effective delivery into the brain and prolonged circulation time of DFO. The nanoparticle delivers the iron chelator across the BBB, possibly through the specific affinity between RVG29 and its possible receptor on the brain microvascular endothelium, which also mediates the subsequent internalization of nanoparticles into the neurons, allowing the drug to remove the excess cellular iron and reduce iron-related oxidative stress (Scheme 1). Impact of the DFO-loaded nanoparticles on the brain iron content, PD-related neurobehavioral defects, and dopaminergic neuron damage of mice was tested in a MPTP-induced PD model. The RNP-DFO nanoformulation significantly enhanced the accumulation of DFO in the brains of mice and effectively decreased their cerebral iron content and ROS level. Administration of RNP-DFO in PD mice also significantly

DOI: 10.1021/acsnano.7b08172
ACS Nano XXXX, XXX, XXX−XXX

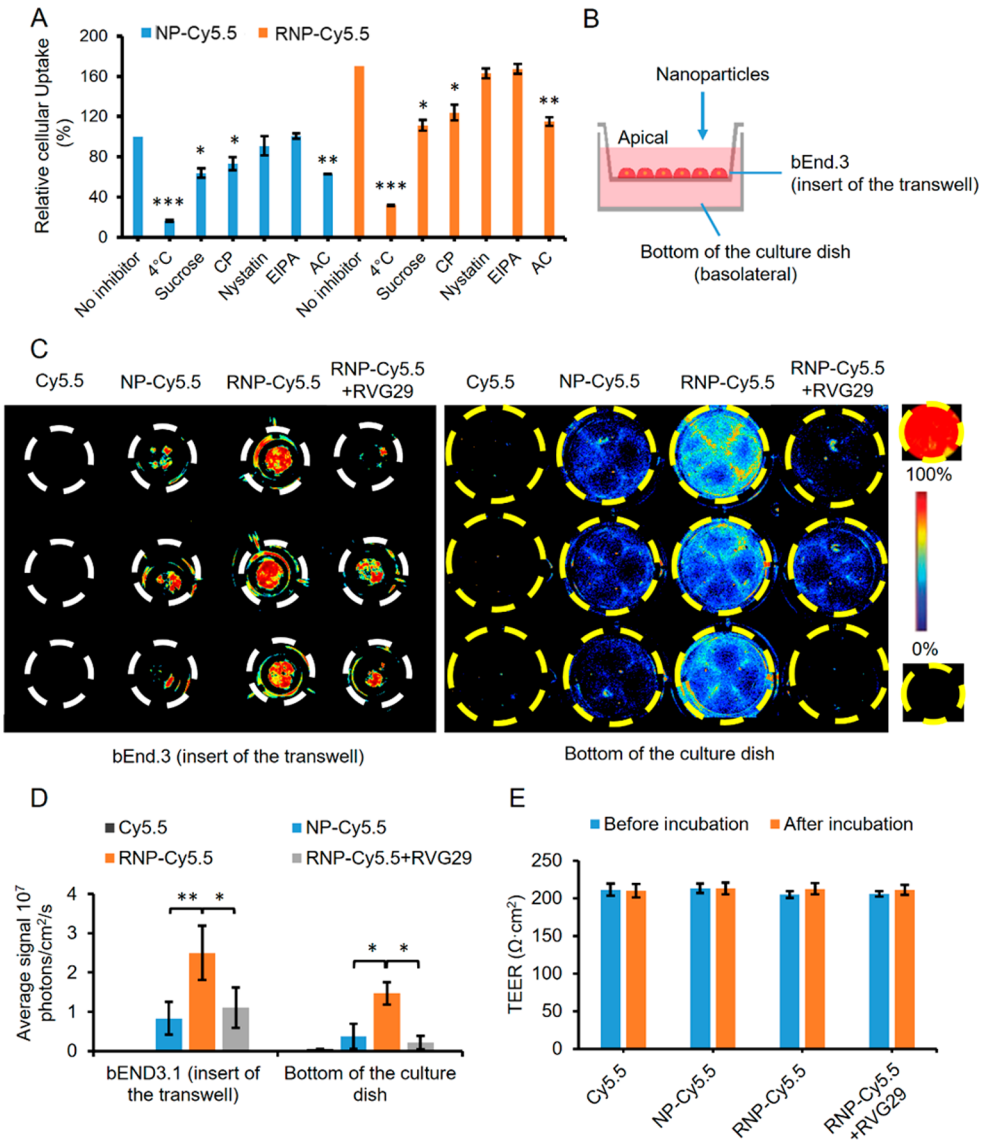

Figure 2. Cellular internalization pathways and blood brain barrier permeability of nanoparticles *in vivo*. (A) Effect of different inhibitors on the internalization of NP-Cy5.5 and RNP-Cy5.5 by bEnd.3 after 4 h incubation at 37 °C, as determined by flow cytometry. Incubation at 4 °C was used to inhibit endocytosis; sucrose and chlorpromazine (CP), clathrin-mediated endocytosis; nystatin, caveolae/lipid raft-mediated endocytosis; EIPA, macropinocytosis; ammonium chloride, lysosome function. Fluorescence intensities are normalized against that of cells incubated with NP-Cy5.5 without inhibitor at 37 °C and presented as mean ± SD ($n = 3$); *$p < 0.05$; **$p < 0.01$; ***$p < 0.001$. (B) Schematic representation of the *in vitro* blood brain barrier penetration test. A tight bEnd.3 monolayer (transendothelial electrical resistance >200 Ω cm^2) was grown on the inset of a transwell dish, and nanoparticles were added to the apical media and allowed to penetrate into the basolateral chamber. (C) Fluorescence images of the bEnd.3 monolayer and the basolateral chamber after 4 h incubation with Cy5.5, NP-Cy5.5, RNP-Cy5.5, or RNP-Cy5.5 with RVG29. Blank medium and medium containing free Cy5.5 (concentration identical to that used in the experiment) served as references for 0 and 100% fluorescence, respectively. White circles indicate the inset of the transwell. Yellow circles indicate the bottom of transwell dish. (D) Average relative fluorescence estimated from images in (C). Data are presented as the mean ± SD; *$p < 0.05$; **$p < 0.01$. (E) Transendothelial electrical resistance (TEER) of the bEnd.3 monolayer measured before and after incubation with Cy5.5, NP-Cy5.5, RNP-Cy5.5, or RNP-Cy5.5 with RVG29. Data are presented as the mean ± SD ($n = 3$).

reduced the damage of dopaminergic neuron in their brain and reversed their neurobehavioral deficits. The nanoparticles had caused no observable brain cell apoptosis or other adverse effects in nontargeted organs *in vivo*. This approach for delivering DFO to the brain may be applied for safe and effective administration of iron chelators for PD treatment.

RESULTS AND DISCUSSION

Characterization of DFO-Encapsulated Nanoparticles and Their Drug Release Profile. The polymeric nanoparticles used in this work were prepared using amphiphilic copolymer mPEG−PLGA, a well-established biodegradable material widely used for drug delivery. The core nanoparticles (NP-DFO) were prepared using a double emulsion method,[29,30] with the hydrophilic drug DFO loaded in the hydrophilic core. The brain-targeting peptide RVG29 was then covalently conjugated to the nanoparticles through a reaction between the maleimide groups on the nanoparticle surface and thiol groups from the peptide. Nuclear magnetic resonance (NMR) results showed that, after conjugation, while the peak for the repeat units of PEG

DOI: 10.1021/acsnano.7b08172
ACS Nano XXXX, XXX, XXX−XXX

Table 2. Characterization of Nanoparticles before and after bEnd.3 Cell Monolayer Penetration and Apparent Permeability Coefficient Calculation[a]

	size (nm)		PDI		ξ (mV)		
	apical	basolateral	apical	basolateral	apical	basolateral	P_{app} ($\times 10^{-5}$ cm/s)
NP-Cy5.5	165.9 ± 1.4	164.2 ± 1.3	0.170 ± 0.021	0.198 ± 0.022	−25.53 ± 0.22	−24.23 ± 1.33	2.12 ± 1.06
RNP-Cy5.5	165.8 ± 1.7	166.3 ± 1.1	0.198 ± 0.044	0.183 ± 0.012	−23.21 ± 0.67	−24.14 ± 2.03	6.54 ± 1.58*

[a]Nanoparticles were incubated with bEnd.3 cell monolayer grown on a transwell insert for 4 h. PBS media were collected from both apical and basolateral chambers, and the contained nanoparticles were subjected to size (diameter, nm), polydispersity index (PDI), and ζ-potential (ξ) measurements. P_{app}, apparent permeability coefficient values of nanoparticles recovered in the basolateral side. Data are presented as the mean ± SD (n = 3)' *p < 0.05.

(3.6 ppm) was still present, the maleimide peak in maleimide−PEG−PLGA (6.7 ppm) disappeared (Figure S1). This verified that RVG29 has been successfully conjugated to the nanoparticles through the maleimide groups. The conjugation efficiency of the RVG29 peptide was estimated as 43.4 ± 3.6%, and the average density of the peptide on the nanoparticle surface was approximately 319 peptide ligands per particle.

The DFO-loaded nanoparticles were then characterized for their morphology, surface charge, drug loading, and release properties. The mean hydrodynamic diameter of NP-DFO was measured by dynamic light scattering (DLS) to be 167.2 ± 1.7 nm, and their ζ-potential is −28.70 ± 0.22 mV. The size and surface charge remained approximately unchanged after RVG29 conjugation as the hydrodynamic diameter and ζ-potential of RNP-DFO were 168.8 ± 1.9 nm and −27.40 ± 0.71, respectively. The RNP-DFO nanoparticles also showed a low polydispersity index (PDI), indicating the uniformity in size (Table 1). Transmission electron microscopy (TEM) characterization confirms that both NP-DFO and RNP-DFO showed uniform spherical morphology (Figure 1A). In addition, the size of the nanoparticles showed no significant change after incubation in phosphate buffer saline (PBS) for 3 days at pH 7.4 (Figure 1B), indicating their high stability.

The encapsulation and loading efficiencies of DFO in RNP-DFO nanoparticles were 45.2 ± 2.8 and 9.2 ± 0.9%, respectively (Table 1). The drug release profiles of DFO from both NP-DFO and RNP-DFO were investigated in PBS at pH 4.4 or pH 7.4. The two nanoparticles showed almost identical drug release profiles, with low pH stimulation drug release (Figure 1C,D). At pH 7.4, about 45% encapsulated DFO was released within 24 h, whereas at pH 4.4, in 24 h, about 75% accumulative drug release was achieved. The enhanced drug release at lower pH may cause the nanoparticles to discharge their cargo in the acidic environment in lysosomes after uptake by the brain cells.

Cellular Internalization of Nanoparticles. To investigate the interactions between nanoparticles and brain cells, essential for its proper functioning *in vivo*, we have first studied their cellular internalization mechanism. Florescent dye Cy5.5 instead of DFO was loaded into the nanocarriers with or without RVG29 conjugation described above, and the resulting nanoparticles (RNP-Cy5.5 and NP-Cy5.5) have properties comparable to those loaded with DFO. Flow cytometry analysis demonstrated that the uptake by brain capillary endothelial cell line bEnd.3 of RNP-Cy5.5 was significantly higher compared to that of NP-Cy5.5, probably due to RVG29-mediated internalization. The fact that the uptake by bEnd.3 of both nanoparticles was dramatically inhibited (by more than 80%) at 4 °C compared to 37 °C (Figure 2A) suggests that their internalization was primarily mediated by the energy-dependent endocytosis rather than energy-independent mechanisms.[31,32] By applying inhibitors specific to different endocytic pathways[33] to the bEnd.3 cells (Figure 2A), it could be observed that two inhibitors of clathrin-coated vesicle formation, sucrose and chlorpromazine,[34,35] both reduced the cellular uptake of the two nanoparticles over 30%, significantly more than any other specific inhibitors. This identified clathrin-mediated endocytosis as the preferential pathway involved in the internalization of NP or RNP. In contrast, little or no impact was detected on the nanoparticle uptake for caveolae-mediated endocytosis inhibitor nystatin and macropinocytosis inhibitor 5-(*N*-ethyl-*N*-isopropyl)amiloride (EIPA),[36] suggesting minimal involvement of these pathways. These results are consistent with previous reports that clathrin-coated vesicles mediate the internalization of particles with a size between 100 and 200 nm,[37,38] which is precisely the size range of our nanoparticles. A previous study also reported that the clathrin-dependent pathway may participate in the internalization of RVG29-conjugated nanoparticles.[26] We have also verified the participation of endosomes/lysosomes in the cellular uptake using the lysosomotropic agent ammonium chloride.[39] An uptake reduction of more than 30% was observed for both NP-Cy5.5 and RNP-Cy5.5 (Figure 2A). This confirmed that these compartments also played a role in the uptake of the nanoparticles. Moreover, the endosomal trafficking may be involved in the transportation of intact particles across the cell barrier, and lysosomes are expected to be responsible for particle degradation and drug release.[38]

Blood Brain Barrier Permeability Studies *in Vitro*. The RVG29-mediated transcytosis of nanoparticles across a capillary endothelial bEnd.3 cell monolayer was then studied as an *in vitro* model for the BBB penetration of nanoparticles.[23,24,40] NP-Cy5.5 and RNP-Cy5.5 were incubated with a compact monolayer of bEnd.3 cells grown on a transwell insert, and both the insert (after wash) and the bottom chamber were imaged for fluorescence (Figure 2B). The results showed that after 4 h of RNP-Cy5.5 incubation, the fluorescence signals in the bEND.3 cell monolayer (insert) and in the lower chamber were, respectively, 3 and 4 times higher than those after incubation with NP-Cy5.5 (Figure 2C,D). However, this difference disappeared when free RVG29 peptide was co-incubated with RNP-Cy5.5 (Figure 2C,D), implying that specific interactions between the nanoparticle-conjugated RVG29 and bEnd.3 cells were responsible for the enhanced penetration of RNP-Cy5.5 across the BBB-mimicking cell monolayer. No significant changes of transendothelial electrical resistance (TEER) were detected for the compact monolayer after incubation with any of these formulations (Figure 2E), indicating that such treatment did not affect its integrity. DLS analysis of the apical and basolateral media demonstrated that the size and surface charge of the nanoparticles present in the basolateral chamber after 4 h of incubation resembled those in the apical medium (Table 2), indicating that intact nanoparticles are able to cross the cell monolayer without being degraded inside cells. The calculated

DOI: 10.1021/acsnano.7b08172
ACS Nano XXXX, XXX, XXX−XXX

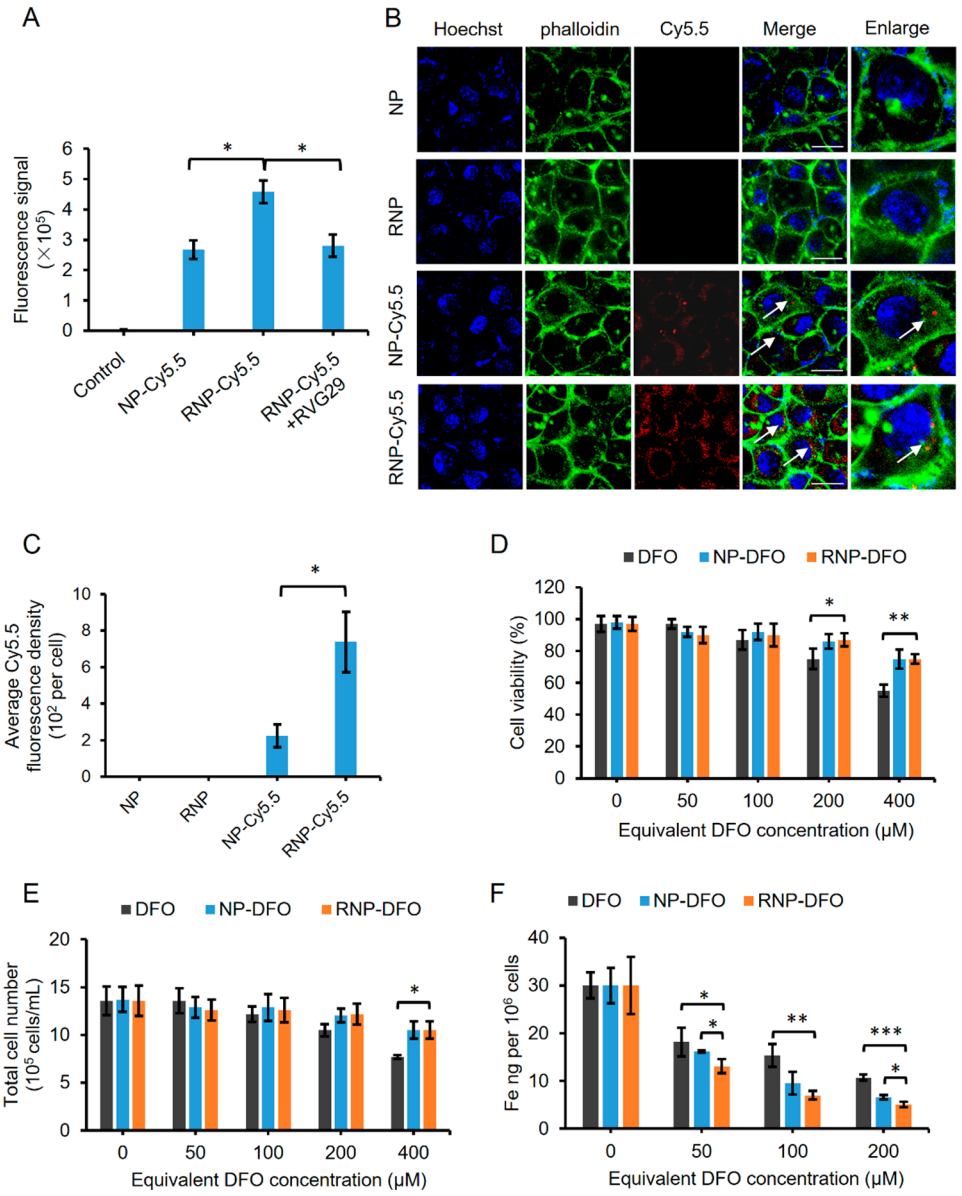

Figure 3. Biological effects of RVG29-modified nanoparticles on SH-SY5Y human neuroblastoma cells. (A) Cellular uptake by SH-SY5Y cells of nanoparticles as determined by flow cytometry after 4 h exposure to NP-Cy5.5, RNP-Cy5.5, or RNP-Cy5.5 and free RVG29 peptide. RVG29 conjugation significantly enhanced the uptake of nanoparticles. Data are presented as mean ± SD ($n = 3$); *$p < 0.05$. (B) Representative confocal images of SH-SY5Y cells after 6 h incubation with Cy5.5. The cells were visualized using FITC-phalloidin (green) for cytoskeleton and Hoechst 33342 (blue) for the nuclei. Enlarged details are shown in the last column to better visualize the presence of nanoparticles (red; white arrows). Scale bar = 20 μm. (C) Quantitative analysis of the Cy5.5 fluorescence density from results of (B) using ImageJ 1.43u software. Data are presented as mean ± SD from five independent quantifications (each includes 20 randomly selected cells); *$p < 0.05$. Cell viability (D), total cell number (E) and cellular iron content (F) of SH-SY5Y cells was detected by CCK8, cell count system, and ICP-MS, respectively, after treatment with free DFO, NP-DFO, and RNP-DFO containing different DFO concentrations. Data are presented as mean ± SD ($n = 6$); *$p < 0.05$; **$p < 0.01$; ***$p < 0.001$.

apparent permeability coefficients (P_{app}) confirmed a significant (3-fold) increase of permeation across the bEnd.3 cell monolayer of RNP-Cy5.5, compared to NP-Cy5.5 (Table 2). These suggested that the conjugation of RVG29 with nanoparticles could significantly enhance their permeability across the endothelial cell barrier *in vitro*, showing its potential for effective brain drug delivery.

RVG29 Enhances the Uptake of Nanoparticles in Neuron Cells. In addition to mediating its penetration across brain capillary endothelial cell barriers, the binding of RVG29 to extracellular surface receptors such as nAchR was also reported to stimulate its subsequent neural uptake.[41] Therefore, we have examined whether RVG29 was able to increase nanoparticle uptake in human neuroblastoma cell line SH-SY5Y. The cells were incubated with NP-Cy5.5 and RNP-Cy5.5 up to 4 h, and the internalization was analyzed by flow cytometry. The high mean fluorescence intensity (MFI; in comparison to control cells) of the cells exposed to RNP-Cy5.5 was more than 40% higher than that of the cells treated with NP-Cy5.5 (Figure 3A). This difference disappeared in the presence of free RVG29 peptide (Figure 3A), confirming that the specific binding of RVG29 to the neuron cells contributed to the cellular uptake of the RVG29-

DOI: 10.1021/acsnano.7b08172
ACS Nano XXXX, XXX, XXX−XXX

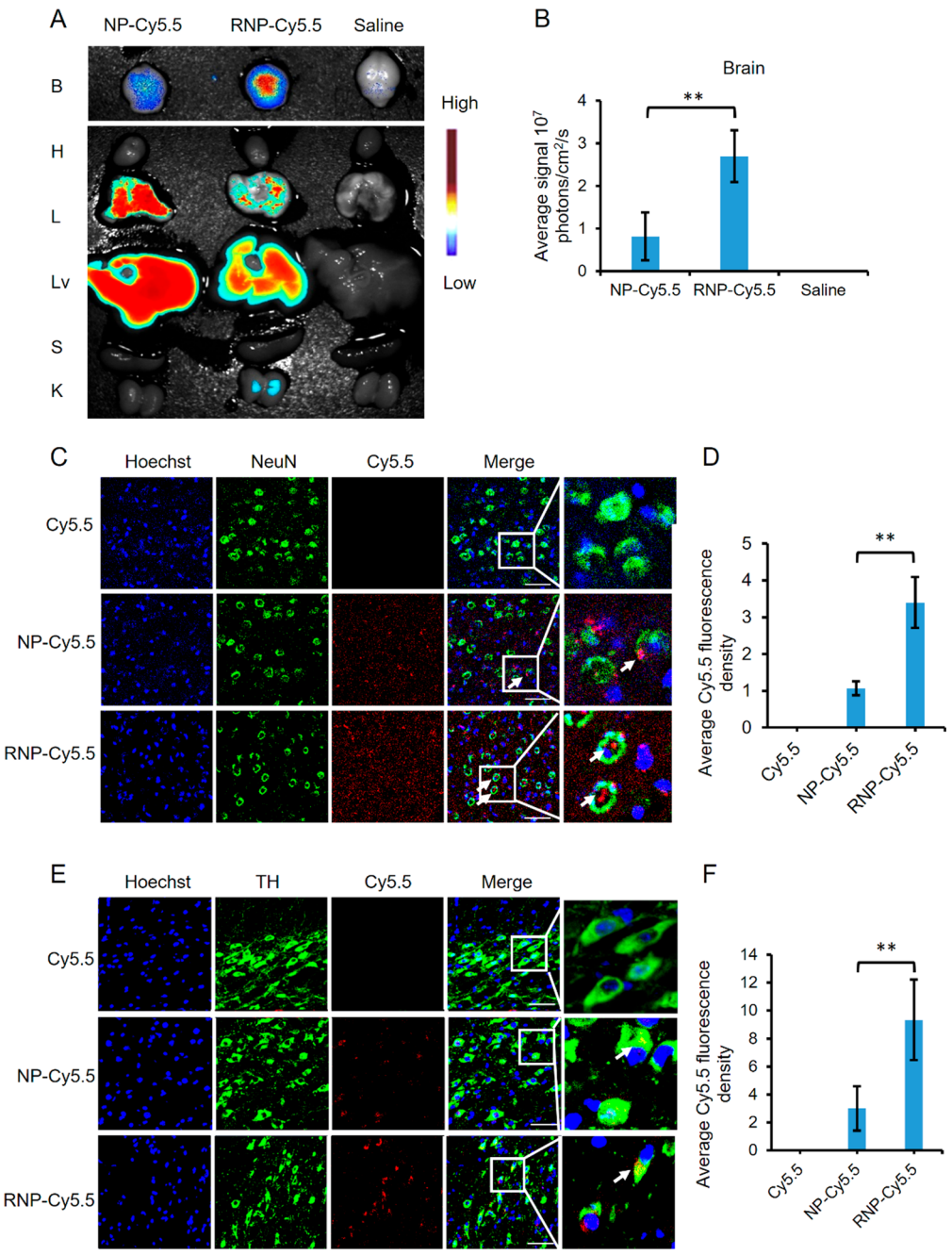

Figure 4. ***In vivo*** **brain targeting of RVG29-modified nanoparticles. (A)** ***Ex vivo*** **fluorescence images of the brain and other major organs from mice treated intravenously with saline, NP-Cy5.5, or RNP-Cy5.5 for 6 h. (B) Average of fluorescence intensities at the brain sites were quantified 6 h postinjection. Data are presented as mean ± SD ($n = 3$); $^{**}p < 0.01$. (C–F) Representative confocal images of striatum (C) and substantia nigra (E) derived from mice treated with Cy5.5, NP-Cy5.5, and RNP-Cy5.5 6 h postinjection. The neurons were visualized using immunostaining (green) for NeuN (striatum) or tyrosine hydroxylase (TH; substantia nigra), and the nuclei were stained with Hoechst 33342 (blue). Enlarged details in the last column show the presence of nanoparticles (red) in the neuron cells. Scale bar = 50 μm. Fluorescence densities in the Cy5.5 channel was quantified in (D) for striatum and (F) for substantia nigra using ImageJ 1.43u. Data are presented as mean ± SD ($n = 3$; five randomly selected views for each animal); $^{**}p < 0.01$.**

coated nanocarrier. The enhanced internalization by neuron cells of RNP-Cy5.5 was also confirmed by fluorescence microscopic measurements (Figure 3B,C). Although substantial incorporation into the cytoplasm occurred for both NP-Cy5.5 and RNP-Cy5.5 following 4 h incubation with SH-SY5Y cells, the internalized amount of RNP-Cy5.5 was notably higher (Figure 3B,C).

RNP-DFO Effectively Removed Intracellular Iron in Neuron Cells with Reduced Cytotoxicity. The biological impact of DFO-loaded nanoparticles on neuron cells after uptake was assessed *in vitro* using cytotoxicity and cellular iron content assays. Cell viability and cell number measurement both showed that free DFO was toxic to SH-SY5Y cells when the concentration reached 200 μM or higher (Figure 3D,E). Meanwhile, the incorporation of DFO into nanoparticles significantly reduced its cytotoxicity, especially at higher equivalent DFO concentrations. No observable alteration in cytotoxicity profile resulted from the conjugation of RVG29 to

DOI: 10.1021/acsnano.7b08172
ACS Nano XXXX, XXX, XXX–XXX

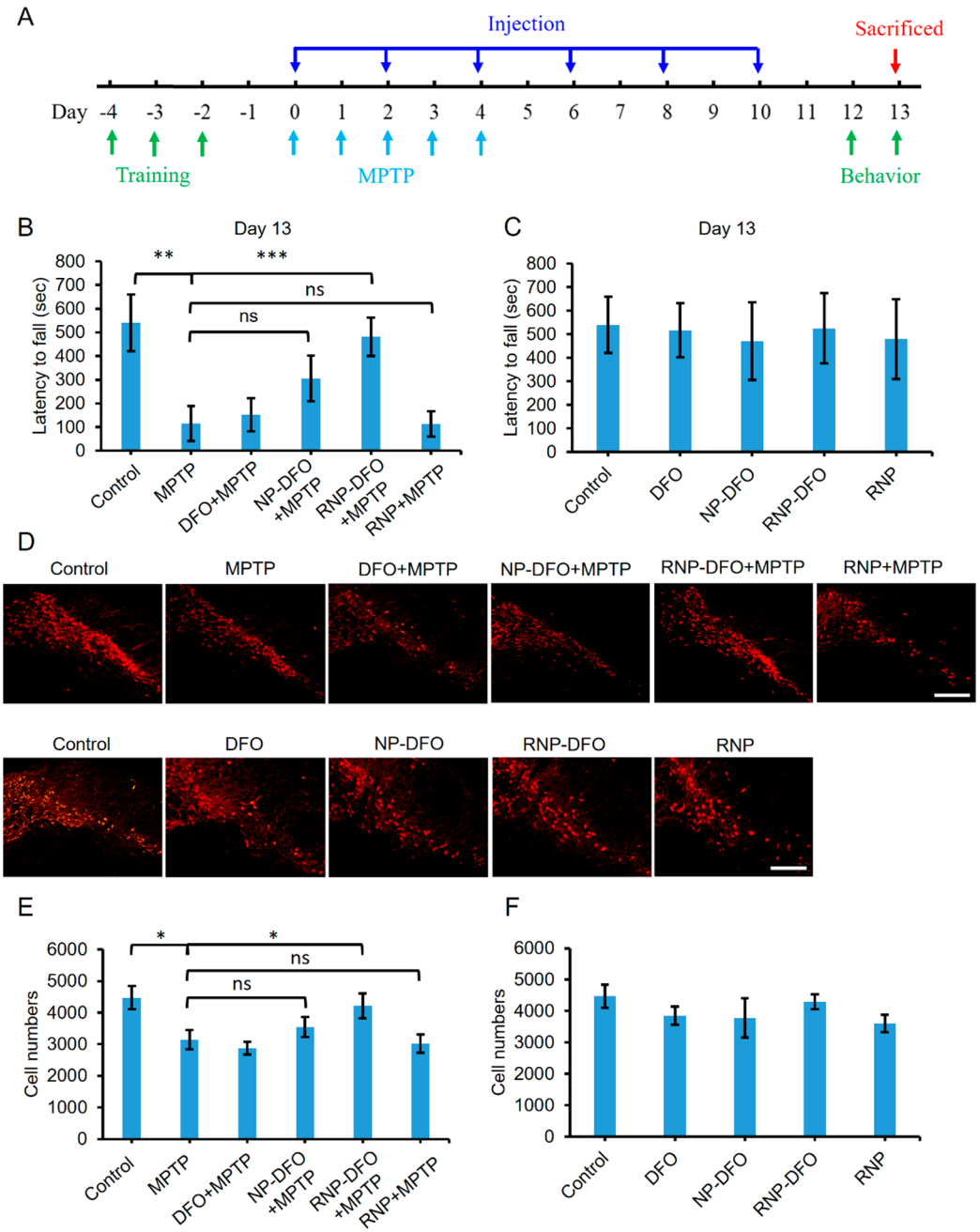

Figure 5. RNP-DFO reduced PD-related neurological damage in mice. (A) Experimental timeline for the construction of an MPTP-induced PD mouse model and the administration of DFO formulations. (B) Behavioral performance of MPTP-induced PD mice on the rotarod after free DFO, NP-DFO, RNP-DFO, or RNP treatment. For mice used as the control, all the injections were replaced with saline. Data are presented as the mean ± SD ($n = 6$); $^{**}p < 0.01$; $^{***}p < 0.001$; ns, nonsignificant. (C) Behavioral performance of normal mice (not induced with MPTP) on the rotarod after treatment with DFO, NP-DFO, RNP-DFO, and RNP following the same timeline in (A). Mice treated with saline were used as the control. Data are presented as mean ± SD ($n = 6$). No significant difference was detected among the four groups. (D) Immunofluorescence staining for tyrosine hydroxylase (TH) in the substantia nigra derived from mice (induced or not induced with MPTP) after DFO, NP-DFO, RNP-DFO, and RNP treatment. Representative images are shown in the same position from bregma. Scale bar = 200 μm. (E,F) Quantification of TH-positive neuron cells in the substantia nigra of PD (E) or normal (F) mice after treatment using an unbiased stereological method. Data are presented as the mean ± SD ($n = 6$); $^{*}p < 0.05$.

nanoparticles. This is possibly due to the gradual release of DFO within the cell from the nanoparticles mitigating its toxic effects.

Iron chelation efficiency of the different DFO formulations was examined by quantification of cellular iron levels. All of the three formulations (free DFO, NP-DFO, and RNP-DFO) removed iron from SH-SY5Y cells. However, RNP-DFO showed the highest iron removal efficiency, significantly superior to free DFO at all the three tested concentrations, and to NP-DFO at concentrations 50 and 200 μM (Figure 3F). These indicated that the use of RVG29-coated nanocarrier significantly enhanced the iron chelation efficiency of DFO in SH-SY5Y cells and decreased its toxicity.

Prolonged Circulation Time of DFO Delivered by Nanoparticles in Comparison to Free Drug. In order to

DOI: 10.1021/acsnano.7b08172
ACS Nano XXXX, XXX, XXX−XXX

verify whether the *in vivo* circulating time of DFO was improved by nanoparticle-based delivery, the time-dependent plasma concentrations of DFO (free drug injected or released from the nanoparticles) following intravenous administration of free DFO, NPs-DFO, and RNP-DFO were studied using female Sprague−Dawley rats (Figure S2). When intravenously injected as free drug, DFO was rapidly cleared from the bloodstream within 30 min. In comparison, both NP-DFO and RNP-DFO delivered drug showed significantly delayed systemic clearance, with detectable DFO present in plasma up to 24 h postinjection. There was no observable difference between the plasma concentration profiles of DFO delivered in the two nanoparticle formulations. This implied that the nanoparticle carrier could significantly increase the circulating time of DFO after intravenous injection, which may be a promising advantage for the potential *in vivo* application of the drug.

***In Vivo* Brain Targeting and Biodistribution of Cy5.5-Loaded Nanoparticles.** To demonstrate the targeting ability of RVG29-coated nanoparticles *in vivo*, C57BL/6 mice were injected through the tail vein with either NP-Cy5.5 or RNP-Cy5.5, and after 6 h, mice were perfused and sacrificed for *ex vivo* imaging. Both nanoparticles visibly accumulated in lung and liver (Figure 4A), which is common for particles of similar size as reported previously.[20] Nonetheless, the mice administered with targeted RNP-Cy5.5 showed fluorescence (3-fold difference) in the brain much higher than that of the nontargeted NP-Cy5.5, and their lung and/or liver signals are also lower than those of the group injected with nontargeted nanoparticles (Figure 4A,B).

To further demonstrate whether the RVG29 peptide is able to mediate the nanoparticles to enter the brain parenchyma rather than staying in microvessels or endothelial cells, we have prepared two nanoparticle formulations loaded with 15 nm gold nanoparticles (nAu) with or without RVG29 conjugation (RNP-nAu and NP-nAu, respectively; Figure S3A). The ability of these formulations to accumulate in the parenchyma of mice was assessed by quantifying the gold content using inductively coupled plasma mass spectrometry (ICP-MS) in brain samples depleted of capillaries after tail vein injection. The results demonstrated that nAu without further encapsulation hardly entered the brain; in both NP-nAu- and RNP-nAu-treated mice, the gold accumulation in parenchyma was much higher than that in blood capillary, and RNP-nAu-treated mice also showed significantly more gold deposition in parenchyma than NP-nAu-treated groups (Figure S3B). These results demonstrated that RVG29 coating could effectively mediate the brain targeting of nanoparticles and had potential for intracerebral drug delivery.

Distribution of Cy5.5-Loaded Nanoparticles in Striatum and Substantia Nigra after Intravenous Administration. To fully perform its therapeutic activity, DFO must be delivered to the striatum and SN region, which are the main brain regions affected by PD. Therefore, we further studied the respective distribution of NP-Cy5.5 and RNP-Cy5.5 in the striatum and SN 6 h after intravenous injection. Fluorescence microscopic analysis showed that both NP-Cy5.5 and RNP-Cy5.5 were able to penetrate into the striatum and SN (no brain penetration after intravenous injection was observed for free Cy5.5). However, the targeted RVG29-modified nanoparticles showed notably stronger accumulation (Figure 4C−F). Additional immunostaining for the neurons was applied to study their colocalization with the nanoparticles. At 6 h postinjection, in both NP-Cy5.5- and RNP-Cy5.5-treated mice, Cy5.5 signals could be localized near or inside the neurons, which confirmed that the nanoparticles were able to reach these cells and possibly implied neural uptake (Figure 4C,E).

RNP-DFO Administration Restored Functional Deficits in MPTP-Induced PD Mice. The *in vivo* efficacy of RNP-DFO was investigated using a well-established MPTP-induced PD mouse model.[7,42] Before treatment, the mice were subjected to three pretraining trials (once per day), and only the behaviorally consistent mice were selected for subsequent experiments. PD syndrome was induced by five intraperitoneal administrations of MPTP. DFO, NP-DFO, and RNP-DFO (equivalent dose of DFO 35 mg/kg) were administered intravenously since the day of the first MPTP injection once every other day for 12 days. The animals were subjected to behavioral testing for 48 h after the final injection (Figure 5A). Impact of the DFO formulations on the PD progress was then assessed according to the behaviors of mice. Compared to normal mice, MPTP-treated mice stayed significantly shorter on the rotating rod due to the PD-related brain damage. However, after being treated with RVG29-DFO, the PD mice could stay much longer on the rotating rod compared to the PD group (average time 482 and 115 s on the 13th day since treatment started, respectively) (Figure 5B). Moreover, the performance of RVG29-DFO-treated mice was approximately identical to that of normal mice (454 s on day 13), suggesting significant improvement in their PD-affected behavior. Free DFO and NP-DFO also increased the average time of PD mice on the rotating rod, but with efficiency significantly inferior to that of RVG29-DFO (Figure 5B). The RNP vehicle cannot increase the average time of PD mice on the rotating rod, indicating that the RVG29-conjugated nanocarrier itself was not able to alleviate behavioral impair in PD mice (Figure 5B). None of the tested formulations showed any discernible impact on the behavior of normal mice in the rotating rod test (Figure 5C). All of these results suggested that using RVG29-functionalized nanoparticles for DFO delivery was able to improve the behavioral deficits in PD mice with efficacy significantly higher than that of free DFO or nontargeted nanoparticles.

One of the characteristic consequences of MPTP-induced injury is the loss of dopaminergic neurons in the SN. Immunoassays confirmed that a significant decrease occurred in the number of tyrosine hydroxylase (TH)-positive neurons as well as the TH protein level in the striatum and SN after MPTP administration (Figure 5D,E and Figure S4). TH is a key enzyme involved in the biosynthesis of dopamine, and its expression is closely associated with dopaminergic neuron function, and the reduction of TH level in the brain tissues is therefore thought to be a direct indication for dopaminergic neuronal loss.[20,43] Both the loss of TH-positive neurons and the reduction of TH level were effectively reversed after RNP-DFO treatment, which showed significantly enhanced efficacy compared to the control formulations (Figure 5D,E and Figure S4). Moreover, none of free DFO, NP-DFO, or RNP vehicle was able to inhibit the loss of TH-positive neurons (Figure 5D,E), although NP-DFO showed limited effect on the TH protein level compared to that of the nontreated control (Figure S4). As in the behavior test, no observable changes in these aspects were caused by any of the formulations in normal mice (Figure 5F and Figure S4). We have next examined the levels of another PD-related protein, α-synuclein, whose elevated expression in SNpc and striatum was also recognized as characteristic in Parkinsonian injury. In PD patients, α-synuclein aggregates to form insoluble fibrils characterized by Lewy bodies.[44] Aggregated α-synuclein interacts with the cell membrane of neurons to form pore-like

DOI: 10.1021/acsnano.7b08172
ACS Nano XXXX, XXX, XXX−XXX

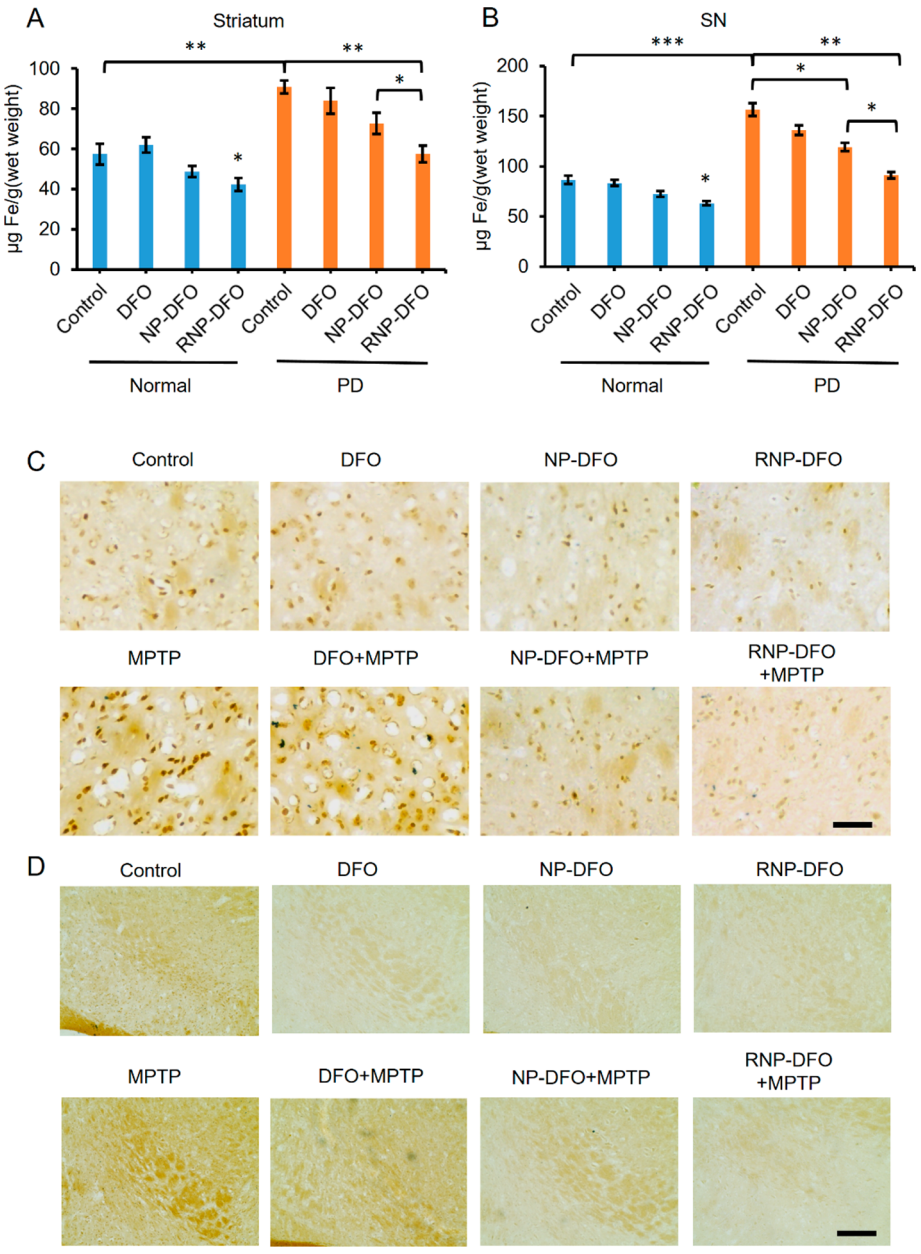

Figure 6. RNP-DFO reduced brain iron content in PD mice. (A,B) Total iron content determined by ICP-MS in the striatum (A) and substantia nigra (B) from normal and MPTP-induced PD mice treated with RNP-DFO and control formulations. Data are presented as mean ± SD ($n = 6$); *$p < 0.05$; **$p < 0.01$; ***$p < 0.001$. (C,D) Immunohistochemistry staining for iron in the striatum (C) and substantia nigra (D) from normal and PD mice after treatment with DFO, NP-DFO, and RNP-DFO. Representative images are shown. Scale bar = 200 μm.

structures and depolarize the membrane potential, which disrupts the normal functions of the cell and leads to dopaminergic neuron death and progress of PD.[44] Some evidence indicates that Fe accumulation in the SN of PD may induce the aggregation of α-synuclein and then cause apoptosis of dopaminergic neuron.[45,46] Western blotting analysis demonstrated that the protein level of α-synuclein in both SN and striatum was significantly increased after MPTP administration, which was effectively reversed by RNP-DFO treatment (Figure S5). In contrast, none of the control formulations (free DFO, NP-DFO, or RNP) was able to reduce the α-synuclein levels in SN or striatum (Figure S5).

To verify the impact of nanoparticle-delivered DFO on the intracerebral deposition of iron, the iron contents in SN and striatum were determined by ICP-MS and immunohistochemistry. Iron accumulated significantly in the two tissues after MPTP treatment (Figure 6A,B). Intravenous administration of DFO did not caused any significant iron reduction in the striatum or SN, and treatment of NP-DFO only showed weak removal efficacy in the SN (but not the striatum) of PD mice (Figure 6A,B). However, the iron contents in MPTP-damaged striatum and SN significantly decreased (by 30 and 40%, respectively) after RNP-DFO treatment, which also showed significantly enhanced iron removal efficacy compared to NP-DFO (Figure 6A,B). In addition, the iron levels of DFO- or NP-DFO-treated PD mice did not significantly differ from that of normal mice. RNP-DFO also reduced brain iron in healthy mice not treated with MPTP (Figure 6A,B). The immunohistochemistry results confirmed that the iron content was reduced significantly by RNP-DFO treatment in the striatum (Figure 6C) and SN

DOI: 10.1021/acsnano.7b08172
ACS Nano XXXX, XXX, XXX−XXX

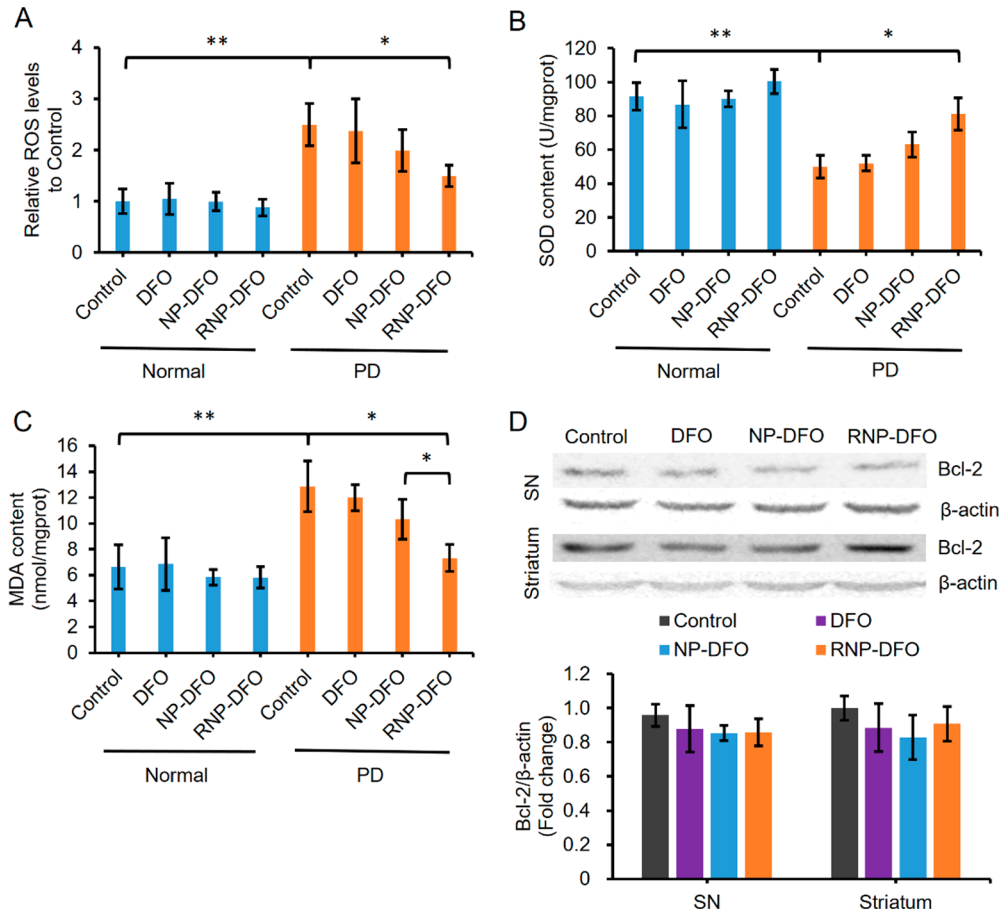

Figure 7. Levels of ROS and Bcl-2 in the brain after intravenous injection of DFO, NP-DFO and RNP-DFO. Levels of (A) reactive oxygen species (ROS), (B) super oxide dismutase (SOD), and (C) malondialdehyde (MDA) in substantia nigra of normal and PD mice after treatment with different DFO formulations. Data are presented as mean ± SD (n = 6); *p < 0.05; **p < 0.01. (D) Western blot analysis of Bcl-2 protein in the striatum and substantia nigra with β-actin used as reference (representative blots, top). The results were normalized using ImageQuant software. Data are presented as mean ± SD (n = 6).

(Figure 6D) of MPTP-treated mice, compared to the other controls. These all suggested that RNP-DFO was able to efficiently remove the excess iron in SN and striatum of MPTP-induced PD mice and showed promising efficacy in reducing the dopaminergic neuron death in their brain and restoring their behavior deficits.

RNP-DFO Administration Reduced the Oxidative Stress in Substantia Nigra in MPTP-Induced Mouse Model of PD. One of the probable mechanisms underlying the neural toxicity of excess iron deposition is that excess iron may generate ROS, which would consequently lead to neuronal death.[8] Therefore, we have also detected the ROS levels in SN after treatment with RNP-DFO or the control formulations (Figure 7A). The results showed that ROS generation in SN derived from PD mice indeed decreased significantly after RNP-DFO treatment, while neither free DFO or NP-DFO has any observable impact. None of the DFO formulations have affected the level of ROS in normal SN (Figure 7A). Similar results were also observed for other oxidative stress indicators, super oxide dismutase (SOD; Figure 7B) and malondialdehyde (MDA; Figure 7C). In normal mice, the Bcl-2 protein levels in the striatum or SN were not significantly changed after nanoparticle treatment, indicating that RNP-DFO itself did not cause cell apoptosis in these tissues (Figure 7D).

Biocompatibility of RNP-DFO in Brain and Other Organs. Effects of the penetration of nanoparticles on the integrity of the BBB were first investigated in normal mice using Evans blue dye extravasation. The mice were previously treated with DFO, NP-DFO, RNP-DFO, or RNP vehicle following the same timeline as in the therapeutic studies. As indicated by the amounts of Evans blue that have permeated into the brain tissue, the permeability of the BBB did not significantly change after any of these treatments, indicating that BBB integrity is not damaged (Figure S6). In addition, to assess whether the administration of DFO or nanoparticles may cause undesirable inflammation in the brain, mRNA levels of inflammation factors including TNF-α, IL-1β, and IL-6 were analyzed in both SN and striatum derived from normal mice treated with different DFO formulations. The results showed that no detectable inflammatory change was observed in these tissues following NP-DFO and RNP-DFO administration (Figure 8A–F).

As we have previously observed that, apart from the brain, the Cy5.5-loaded nanoparticles were also located in the liver, lung, and kidney of animals 6 h after intravenous administration, a further histopathological analysis was performed to investigate the impact of DFO nanoformulation on the nontargeted organs. H&E staining results indicated that no detectable pathological change was observed in the major organs derived from normal mice following NP-DFO and RNP-DFO administration (Figure 9A) or in their serum biochemical indicators of liver or kidney function (Figure 9B–E). In contrast, free DFO treatment resulted in observable kidney and liver injury such as fat

DOI: 10.1021/acsnano.7b08172
ACS Nano XXXX, XXX, XXX–XXX

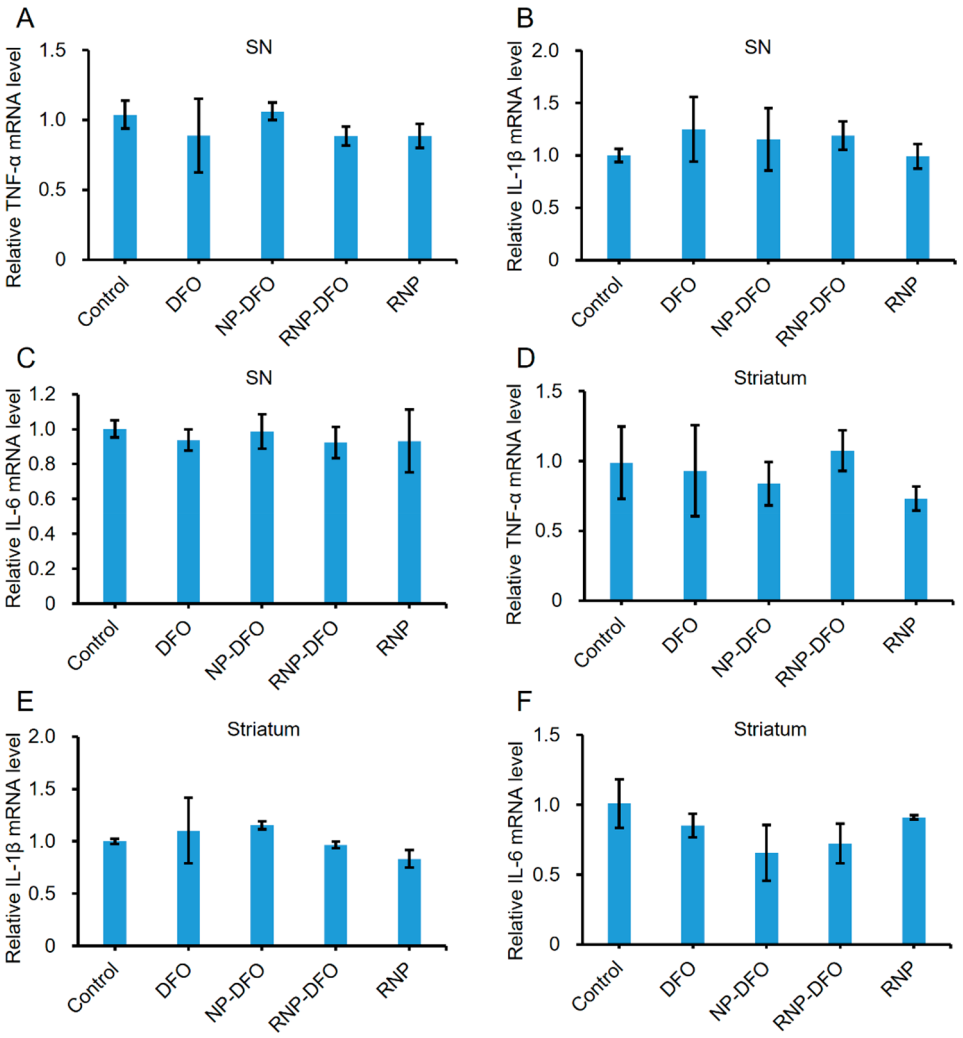

Figure 8. RNP-DFO induced no overt neuroinflammation in SN and striatum. Quantitative measurement of IL-1β, TNF-α, and IL-6 mRNA in SN (A–C) and striatum (D–E) of normal mice was carried out after treatment with different DFO formulations. The mice were given six intravenous injections once every 2 days and sacrificed on the third day after the last injection. Mice treated with saline were used as the control. Results are displayed as mean ± SD, n = 5.

vacuolation in hepatocytes, renal tubular atrophy and interstitial loosening in the kidney (Figure 9A), and a significant elevation in the serum level of liver function indicator aspartate transaminase (AST; Figure 9B), which is consistent with previous reports that systemic administration of free DFO led to kidney and liver damage.[12] This indicated that RNP-DFO could efficiently reduce brain iron content without causing obvious side effects, which makes it more attractive for the treatment of iron overload in PD.

CONCLUSION

In this work, we reported a biocompatible lipid–polymer hybrid nanoparticle modified with BBB-penetrating peptide RVG29 to deliver iron chelator DFO into the brain for treatment of PD. All biomaterials involved in this nanoparticle were already approved for clinical usage. This nanoparticle system showed satisfactory efficiency in intracerebral delivery of DFO and could be readily internalized by neuron cells. When administered intravenously to MPTP-induced PD mice, this nanoformulation of DFO was able to effectively remove iron from their brain and has significantly prevented the PD-related neuron damage as well as the neurobehavioral deficits, possibly by reducing the iron-mediated oxidative stress. No neuron cell apoptosis or other adverse effects in the major organs were observed after treatment with our nanoparticles. This nanoformulation could be a promising approach for the intracerebral delivery of iron chelators and their potential use for treatment of PD.

EXPERIMENTAL SECTION

Materials. Monomethoxy poly(ethylene glycol) (mPEG)-poly-(lactic-*co*-glycolic acid) (PLGA; molar ratio of D,L-lactic to glycolic acid, 75:25) and maleimide–PEG–PLGA were purchased from Jinan Daigang Biotechnology Co. Ltd. (Jinan, China). The RVG29 peptide with an additional cysteine on its C-terminal (RVG29-Cys) was synthesized by GL Biochem Ltd. (Shanghai, China). The peptide sequence of RVG29-Cys is YTIWMPENPRPGTPCDIFTNSR-GKRASNGC. Hoechst 33342 and FITC-phalloidin were obtained from Invitrogen (San Diego, CA, USA). All other chemicals and agents were obtained from Sigma-Aldrich (St. Louis, MO, USA) unless otherwise noted. TH primary antibody (ab112) was purchased from Abcam (Cambridge, MA, USA). α-Synuclein (4179) and B cell lymphoma 2 (Bcl-2, 3498) primary antibodies were purchased from Cell Signaling Technology (Danvers, MA, USA). A β-actin primary antibody (A5060) was purchased from Sigma-Aldrich (St. Louis, MO, USA). The secondary antibody of anti-rabbit IgG conjugated to horseradish peroxide (ab6721) was purchased from Abcam (Cambridge, MA, USA). Rhodamine-conjugated goat anti-rabbit IgG

DOI: 10.1021/acsnano.7b08172
ACS Nano XXXX, XXX, XXX–XXX

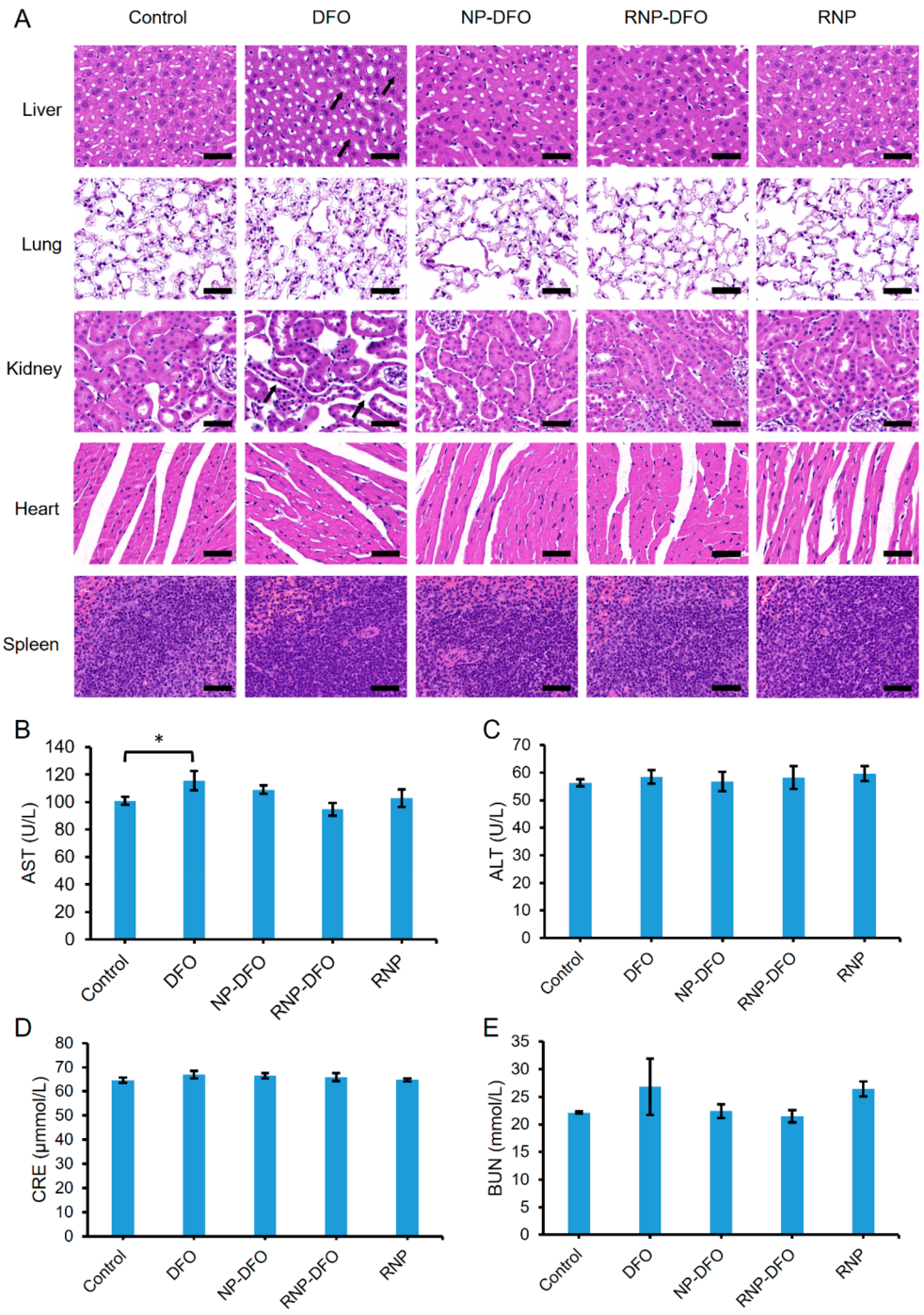

Figure 9. RNP-DFO exerted no observable toxicity in major organs. (A) Representative photomicrographs showing histopathology of the liver, lung, kidney, heart and spleen of control, DFO-, NP-DFO-, and RNP-DFO-infused mice (n = 5). There was no detectable pathological change in the major organs derived from normal mice following NP-DFO and RNP-DFO administration. Free DFO treatment resulted in kidney and liver injury such as fat vacuolation in hepatocyte or renal tubular atrophy and interstitial loosening in kidney. Black arrows indicate the injury sites. (B–E) Serum biochemical analysis of the treated mice (mean ± SD, n = 5); *p < 0.05. (B) AST, aspartate transaminase; (C) ALT, alanine transaminase; (D) CRE, creatinine; (E) BUN, blood urea nitrogen. Mice treated with saline were used as the control.

(AP132R) was purchased from Millipore Corporation (Temecula, CA, USA).

Preparation of Nanoparticles. A double emulsion method was used for the preparation of unmodified nanoparticles.[29] Briefly, 18 mg of mPEG–PLGA and 2 mg of maleimide–PEG–PLGA were dissolved in 1 mL of methylene chloride and mixed with 0.2 mL of water (or aqueous solution of DFO or fluorescent dye Cy5.5 if necessary) following sonication for 5 min. The product was then added to 2 mL of 5% aqueous solution of sodium cholate and sonicated for another 5 min. The new mixture was then slowly pipetted into 10 mL of 0.5% sodium cholate and stirred at room temperature for 20 min. The methylene chloride was removed by vacuum evaporation at 30 °C. The solution were then centrifuged at 12 000g for 30 min at 4 °C, and the harvested nanoparticles were rinsed twice to be resuspended in triple-distilled water.

RVG29 peptide was conjugated to the nanoparticles prepared as above *via* a maleimide–thiol reaction between maleimide–PEG–PLGA and RVG29-Cys. The nanoparticles were mixed with an excess amount

DOI: 10.1021/acsnano.7b08172
ACS Nano XXXX, XXX, XXX–XXX

of RVG29-Cys and incubated in PBS for 8 h at room temperature. The unconjugated peptide was removed from the reaction system *via* centrifugation, and the resulting nanoparticles were washed twice with distilled water. The unmodified nanoparticles were also incubated with PBS not containing RVG29-Cys for 8 h and washed as described above before any further characterization or other experiments.

Evaluation of RVG29 Conjugation Efficiency and RVG29 Density on Nanoparticle Surface. Aliquots of RNP or NP were dissolved in pH 7.4 PBS, and the concentration of RVG29 peptide was determined using a BCA assay. The conjugation efficiency (CE) of RVG29 was calculated as

$$\mathrm{CE}(\%) = \text{amount of conjugated RVG29} / \text{total amount of peptide added} \times 100\%$$

Surface density of RVG29 was determined by dividing the estimated number of RVG29 molecules by the number (n) of nanoparticles using the following equation:

$$n = 6 \times \text{nanoparticle weight} / (\pi \times \text{number mean nanoparticle diameter}^3 \times \rho)$$

where ρ represents the nanoparticle weight per volume unit, approximated to be 1.1 g/cm^3.[47]

Nuclear Magnetic Resonance (NMR) Analysis. Nanoparticles with or without RVG29 conjugation were dissolved in deuterated chloroform and analyzed by a Varian NMR (Palo Alto, CA, USA) to confirm the linkage between RVG29-Cys and maleimide−PEG−PLGA.

Transmission Electron Microscopy (TEM). Nanoparticles stained with 2% uranyl acetate solution for 5 min were deposited on a carbon-coated copper grid and characterized using a JEM-200CX transmission electron microscope (Jeol Ltd., Japan).

Determination of Nanoparticle Size and ζ-Potential. The hydrodynamic diameter, size distribution, and ζ-potential of the nanoparticles were measured using a ZetaSizer Nano series Nano-ZS (Malvern Instruments Ltd., Malvern, UK). Samples were measured at 25 °C.

Determination of DFO Loading and Encapsulation Efficiency. The NP-DFO and RNP-DFO nanoparticles were treated with dichloromethane to break down the mPEG−PLGA shell and release DFO. Then dichloromethane was removed by rotary evaporation, and DFO was dissolved in triple-distilled water. To the extracted solution was added 10 mM ferric chloride ($FeCl_3$) solution of identical volume, and the absorbance of the resulting DFO−Fe compound was determined at 430 nm using a Lambda 950 UV−vis spectrophotometer.

The loading efficiency and encapsulation efficiency were calculated as

$$\text{loading efficiency (LE)} = \text{weight of DFO in nanoparticles} / \text{weight of nanoparticles} \times 100\%$$

$$\text{encapsulation efficiency (EE)} = \text{weight of DFO in nanoparticles} / \text{weight of total DFO} \times 100\%$$

Drug Release Profile of RNP-DFO. Release kinetics of DFO under mimic physiological conditions from RNP-DFO were measured using a dialysis method. In brief, 20 mg of RNP-DFO was suspended in 1 mL of PBS (pH 4.4 or 7.4) in a dialysis bag with a molecular weight cutoff of 18 kDa. The solution was dialyzed against 10 mL of PBS (pH 7.4 or 4.4) under 100 rpm stirring at 37 °C. At different time points, the PBS was collected and incubated with excess $FeCl_3$, and the absorbance of resulting DFO−Fe compound was measured at 430 nm to determine the concentration of DFO in solution using a standard curve of DFO−Fe in PBS.

Cell Culture. SH-SY5Y cells and bEnd.3 cells were cultured in DMEM containing 10% FBS, 100 U/mL penicillin, and 100 μg/mL streptomycin. Cells were placed in an incubator at 37 °C with 5% CO_2 and 99% humidity.

Cellular Internalization of NPs. Uptake of NPs into neuronal cells was investigated using Cy5.5-loaded nanoparticles (NP-Cy5.5 or RNP-Cy5.5). SH-SY5Y cells (4×10^5 cells per well) were cultured in a six-well culture plate. Before use, the fluorescence of the NP-Cy5.5 and RNP-Cy5.5 nanoparticles was quantified by an F-4600 FL spectrophotometer (Hitachi, Japan). Cells were incubated with NP-Cy5.5, RNP-Cy5.5, or RNP-Cy5.5 with free RVG29 peptide suspended in DMEM culture medium (containing 75 ng of Cy5.5) for 6 h. For flow cytometry, unbound NPs were removed by washing the cells twice with PBS, and the cells were harvested and resuspended in PBS. Flow cytometry (Becton Dickinson, San Jose, CA) was performed in the FL4 channel using an argon 630 laser.

For fluorescence microscopy analysis, after incubation with NPs, NP-Cy5.5, or RNP-Cy5.5 for 6 h, the cells were fixed with 4% paraformaldehyde at room temperature for 30 min. The fixed cells were permeabilized with 0.1% Triton X-100 for 1 min and then incubated with FITC-phalloidin solution (1:2000) for 40 min. Hoechst 33342 was used to stain the nuclei for 5 min. The cells were observed with an LSM 710 confocal microscope (Carl Zeiss, USA).

Internalization Pathways. The pathways involved in the internalization of nanoparticles by brain cells were studied by preincubating bEnd.3 cells (2×10^5 cells per well) for 2 h with two different inhibitors: 0.45 M sucrose or 30 μM chlorpromazine for clathrin-mediated endocytosis; 100 μM EIPA for macropinocytosis; 30 μM nystatin for caveolae-mediated endocytosis; and 1 mg/mL ammonium chloride for lysosome inhibition. Cells were also incubated at 4 °C to minimize all energy-dependent pathways. Then cells were treated with Cy5.5-labeled NPs for 4 h and analyzed after being washed twice. The Cy5.5 fluorescence was detected by flow cytometry. Cells incubated without inhibitor were used as the negative control.

Blood Brain Barrier Permeability *in Vitro*. bEnd.3 (1×10^5 cells per polyester transwell insert) was cultured in 6 wells (pore diameter of 0.4 μm, 4.67 cm^2). After 7 days, the cells reached confluence, and the resulting monolayer was thought to reasonably mimic the BBB morphology and activity *in vitro*.[35,48] To monitor the tightness of the monolayer, its TEER was detected by a Millicell-ERS volt-ohmmeter (Millipore Co., USA). The monolayer of cells with at least 200 Ω·cm^2 TEER was selected for further experiments.[49] To evaluate nanoparticle penetration across this monolayer, the culture media were replaced with PBS, and RNP-Cy5.5 or NP-Cy5.5 (equivalent amounts of Cy5.5 dye) was incubated on the apical side for 4 h. The fluorescence in the bEnd.3 (insert of the transwell) layer and in the bottom chamber was imaged using a CRi fluorescent imaging system (Woburn, MA, USA). The PBS media in both apical and basolateral chambers were collected, and the hydrodynamic diameter and ζ-potential of the contained particles were analyzed as described above. The concentration of Cy5.5 was measured by fluorescence spectroscopy (675/695 nm), and the apparent permeability coefficients (P_{app}) of nanoparticles were determined as

$$P_{app}\ (\mathrm{cm/s}) = (Q/t) \times (1/A) \times (1/C)$$

where Q represents the total amount of permeated Cy5.5 (μg), A is the surface area of the filter (cm^2), C is the initial Cy5.5 concentration (μg/cm^3), and t is the experiment time (s).

Cell Viability Assay. SH-SY5Y cells (1×10^4) were seeded in 96-well plates and incubated with DFO, NP-DFO, and RNP-DFO (0, 50, 100, 200, or 400 μM) for 24 h. A cell counting kit-8 assay (Dojindo Laboratories, Kumamoto, Japan) was used for cell viability measurement.

For the counting of total cell numbers, after incubation with different DFO formations, incubation SH-SY5Y cells were collected in 1 mL of PBS and then incubated with 0.4% Trypan blue. The live cells (not stained) were counted using a hemocytometer.

Plasma Pharmacokinetics of Free DFO, NP-DFO, and RNP-DFO. NP-DFO, RNP-DFO (equivalent to 50 mg/kg DFO), and free DFO (50 mg/kg) was intravenously administered to female Sprague−Dawley rats (170 ± 10 g) (n = 4). Blood samples were harvested from the tail vein at 0.08, 0.5, 1, 2, 4, 6, 12, and 24 h post-dosing into heparinized microcentrifuge tubes. The blood samples were centrifuged at 1000g for 15 min at 4 °C.

For plasma DFO quantification, the plasma sample was mixed with an equivalent volume of 10 mM $FeCl_3$ aqueous solution, vortexed for 5 min, and centrifuged at 12 000g for 20 min. The supernatant was

DOI: 10.1021/acsnano.7b08172
ACS Nano XXXX, XXX, XXX−XXX

precipitated by ice cold acetonitrile (sample volume/acetonitrile volume 1:4) and centrifuged at 12 000*g* for 20 min again. The supernatant was then analyzed using high-performance liquid chromatography (HPLC).

High-Performance Liquid Chromatography for Quantification of Deferoxamine-Fe. A Waters HPLC system (Waters 2478, Milford, MA, USA) coupled with an autosampler (model 717 plus), a binary pump (model 1525), and a UV photodiode array detector (model 996) was employed. The column used was a symmetry C18 reverse-phase column (Nova-Pak 20 mL, 4.6 × 150 mm, Waters, Milford, MA), and the mobile phase for elution contained 70% acetonitrile and 30% water (v/v). Flow rate was set as 1.0 mL/min, and the eluent was monitored at 430 nm at 25 °C.

Animal Studies. All the animal studies were approved by the Animal Care and Use Committee of Beijing Science and Technical Bureau. Male C57BL/6 mice of approximately 25 g (Beijing Vital River Laboratory Animal Technology Co., Ltd., Beijing, China) were maintained in cages at 21 ± 2 °C in a room with controlled humidity with a 12 h light/dark cycle and provided free access to food and water. All mice were allowed to adapt for 3 days before the experiment started.

The mice that pretrained on the rotating rod and had no difference in time staying on the rod were selected for further studies. For therapeutic studies, the mice were injected with MPTP intraperitoneally five times (35 mg/kg per injection per day) to induce PD. DFO, NP-DFO, RNP-DFO (DFO 35 mg/kg), and unloaded RNP vehicle were injected intravenously once every other day for 12 days as the same day MPTP induction started. DFO concentration was determined for each batch of nanoparticles as described before to control the injected dose. The animals were subjected to behavioral testing 48 h after final injection and then sacrificed.

Evans Blue Extravasation for BBB Permeability Measurement. Normal mice were intravenously treated with DFO, NP-DFO, RNP-DFO (equivalent DFO 35 mg/kg), or RNP vehicle once every other day for 12 days. On the third day after the last injection, they were injected slowly with Evans blue (3% in PBS; 4 mL/kg) through the tail vein and euthanized 2 h later. The mice were then perfused with PBS to remove the free dye. Each hemisphere of the brain was weighed and cut into 2 mm thick sections and then incubated in 1 mL of formamide at 55 °C for 24 h. After centrifugation at 12 000*g* for 20 min, the supernatant was collected and the concentration of Evans blue was quantified using its absorbance at 620 nm.

***In Vivo* Biodistribution Studies.** Normal C57BL/6 mice were injected with NP-Cy5.5 or RNP-Cy5.5 (equal amounts of dye) by tail vein. After 4 h, the brain, heart, lung, liver, spleen, and kidneys of the animals were harvested and imaged using a CRi fluorescent imaging system.

Preparation of Gold-Containing Nanoparticles and Determination of Brain Delivery Efficiency. Gold nanoparticles (nAu, approximately 15 nm in diameter) were synthesized as described previously.[50] NP-nAu and RNP-nAu were then prepared using the same protocol described above replacing the 0.2 mL of DFO solution with gold nanoparticles dispersed in 0.2 mL of water. The mice were administered with nAu, NP-nAu, or RNP-nAu (nAu dose 30 mg/kg as quantified by ICP-MS) through tail vein injection. After 4 h, their brain tissues were harvested, and the brain blood capillaries were depleted from the parenchyma according to a protocol reported before.[51] Briefly, the brain sample was homogenized in a buffer containing 10 mM HEPES, 141 mM NaCl, 4 mM KCl, 1.0 mM $MgSO_4$, NaH_2PO_4, 2.5 mM $CaCl_2$, 1 mM sodium pyruvate, and 10 mM glucose, with pH at 7.4. Dextran was then added until the mass concentration reached 13%, and the mixture was homogenized again. The product was centrifuged at 5800*g* for 20 min, and the supernatant was collected as the parenchyma fraction, and the pellet contained the capillary. Both fractions were digested and subjected to ICP-MS analysis.

Rotarod Performance Test. PD-induced behavioral changes were estimated as described previously.[7] In brief, mice performed three 10 min pretraining trials daily for 3 consecutive days before MPTP treatment. The test instrument (Shandong Medical Academy of Sciences, China) used a rod with a diameter of 3 cm and set at 40 rpm rotation. Mice were placed on the rotating rod, and the time for which each mouse maintained balance on the rod was recorded. Each mouse was tested three times with an intertrial interval of 20 min. The average time was considered as the final scores.

Immunofluorescence. The immunofluorescence analysis was carried out according to previous description.[7] Rabbit anti-mouse TH was used as the primary antibody. Rhodamine-conjugated goat anti-rabbit IgG was used as the secondary antibody. The red fluorescence was imaged using a Zeiss LSM710 microscope.

The number of TH-positive neurons in the SNpc was counted using an effective unbiased stereological method described previously.[52] In brief, 40 consequent slices of cryosection (30 μm in thickness) were collected from AP −2.80 mm to AP −3.97 mm and were counted for quantification of TH-positive neurons in the SNpc of each mouse.[52] The experiment was carried out six times.

Inductively Coupled Plasma Mass Spectrometry. Gold and iron contents in nanoparticles or biological samples were determined using ICP-MS as described elsewhere.[53] For gold content analysis, NP-nAu and RNP-nAu nanoparticles dispersed in triple-distilled water or parenchyma and brain capillary fractions separated as mentioned before were used. For total iron analysis, approximately 20 mg of dried brain tissue or 1 × 10^6 cells (centrifuged from suspended media) was harvested. Digestion was carried out using a total of 1 mL of ultrapure nitric acid (69.9−70.0%, J.T. Baker, USA) and 0.15 mL of H_2O_2, with the microwave digestion process setting at 100 °C for 2 h, followed by 200 °C for 4 h. The digested samples were then dissolved in 3 mL of ultrapure water and subjected to element concentration determination using an X Series 2 ICP-MS (Thermo Fisher, FL, USA).

Iron Histochemistry with Perl's Staining. 3,3-Diaminobenzidine tetrahydrochloride (DAB)-enhanced Perl's staining was used for determination of iron content.[14] Briefly, 15 μm sections were treated with 3% hydrogen peroxide for 10 min. The samples were then treated with Perl's solution for 6 h. After being washed with PBS (pH 7.4), the samples were treated with DAB for 10 min to intensify the dyeing reaction.

Measurement of Oxidative Stress Indicators. Levels of ROS, MDA, and SOD in the brain tissues were determined using commercial kits (E004, A003, A001-1-1, Nanjing Jiancheng Bioengineering Institute, Nanjing, China) according to the manufacturer's protocol.[54]

RNA Isolation and Quantitative PCR (qPCR). Total RNA was isolated from SN or striatum tissues using TRIzol reagent (Invitrogen, San Diego, CA, USA) according to the manufacturer's protocol. A total of 1 μg of total RNA was then used for cDNA first strand synthesis using an M-MLV reverse transcriptase kit (Takara Biotechnology Co., Dalian, China). qPCR was performed to determine the transcriptional levels of IL-1β, TNF-α, and IL-6 using SYBR Green PCR Master Mix (Applied Biosystems, Waltham, MA, USA) in an Applied Biosystems 7500 real-time PCR system. The thermoparameters were set as follows: 95 °C for 10 min, followed by 40 cycles of 95 °C for 5 s and 60 °C for 30 s. Three biological replicates were performed with three technical replicates. β-Actin was used as an internal reference. Primers sequences were as follows: IL-1β forward 5′-GAAATGCCACCTTTTGACAGTG-3′ and reverse 5′-CTGGATGCTCTCATCAGGACA-3′; TNF-α forward 5′-AGGCGGTGCCTATGTCTCA-3′ and reverse 5′-GAGGCCATTTG-GGAACTTCT-3′; IL-6 forward 5′-GCTACCAAACTGGATATA-ATCAGGA-3′ and reverse 5′-CCAGGTAGCTATGGTACT-CCAGAA-3′; β-actin forward 5′-CTCCAGAA-3′ and reverse 5′-TCTCCATGTCGTCCCAGTTG-3′. Relative gene expression levels were determined *via* a $2^{-\Delta\Delta Ct}$ method.

Statistical Analysis. Statistical analysis was performed with SPSS 21.0 software (SPSS Inc., Chicago, IL). Differences were analyzed by one-way ANOVA. Dunnett's test or Student−Newman−Keuls test were used as *post hoc* tests.

ASSOCIATED CONTENT

Supporting Information

The Supporting Information is available free of charge on the ACS Publications website at DOI: 10.1021/acsnano.7b08172.

Figures S1−S6 (PDF)

DOI: 10.1021/acsnano.7b08172
ACS Nano XXXX, XXX, XXX−XXX

AUTHOR INFORMATION

Corresponding Authors

*E-mail: frankyzchang@yahoo.com.hk.
*E-mail: louxin301@gmail.com.
*E-mail: niegj@nanoctr.cn.

ORCID

Xuexiang Han: 0000-0003-0011-5222
Guangjun Nie: 0000-0001-5040-9793

Author Contributions

△L.Y., J.W., and T.L. contributed equally to this work.

Notes

The authors declare no competing financial interest.

ACKNOWLEDGMENTS

This work was supported by the National Natural Science Foundation of China (31730032, 31520103908, 31470969, 31700870), the National Distinguished Young Scientists program (31325010), the Innovation Research Group of the National Natural Science Foundation (11621505), the Key Research Project of Frontier Science of the Chinese Academy of Sciences (QYZDJ-SSW-SLH022), Queensland−Chinese Academy of Sciences (Q-CAS) Collaborative Science Fund QCAS03916-17RD6, and Beijing Municipal Science & Technology Commission (Z161100000116035).

REFERENCES

(1) Sofic, E.; Riederer, P.; Heinsen, H.; Beckmann, H.; Reynolds, G. P.; Hebenstreit, G.; Youdim, M. B. Increased Iron (III) and Total Iron Content in Post Mortem Substantia Nigra of Parkinsonian Brain. *J. Neural Transm* **1988**, *74*, 199−205.

(2) Olanow, C. W.; Stern, M. B.; Sethi, K. The Scientific and Clinical Basis for the Treatment of Parkinson Disease. *Neurology* **2009**, *72*, S1−S136.

(3) Lorincz, M. T. Clinical Implications of Parkinson's Disease Genetics. *Semin Neurol* **2006**, *26*, 492−498.

(4) Sian-Hulsmann, J.; Mandel, S.; Youdim, M. B.; Riederer, P. The Relevance of Iron in the Pathogenesis of Parkinson's Disease. *J. Neurochem.* **2011**, *118*, 939−957.

(5) Han, Y. H.; Lee, J. H.; Kang, B. M.; Mun, C. W.; Baik, S. K.; Shin, Y.; Park, K. H. Topographical Differences of Brain Iron Deposition Between Progressive Supranuclear Palsy and Parkinsonian Variant Multiple System Atrophy. *J. Neurol. Sci.* **2013**, *325*, 29−35.

(6) Walter, U. Transcranial Sonography in Brain Disorders with Trace Metal Accumulation. *Transcranial Sonography in Movement Disorders*; International Review of Neurobiology; Elsevier, 2010; Vol. *90*, pp 166−178.

(7) You, L. H.; Li, F.; Wang, L.; Zhao, S. E.; Wang, S. M.; Zhang, L. L.; Zhang, L. H.; Duan, X. L.; Yu, P.; Chang, Y. Z. Brain Iron Accumulation Exacerbates the Pathogenesis of MPTP-Induced Parkinson's Disease. *Neuroscience* **2015**, *284*, 234−246.

(8) Weinreb, O.; Mandel, S.; Youdim, M. B. H.; Amit, T. Targeting Dysregulation of Brain Iron Homeostasis in Parkinson's Disease by Iron Chelators. *Free Radical Biol. Med.* **2013**, *62*, 52−64.

(9) Sengstock, G. J.; Olanow, C. W.; Menzies, R. A.; Dunn, A. J.; Arendash, G. W. Infusion of Iron into the Rat Substantia Nigra: Nigral Pathology and Dose-Dependent Loss of Striatal Dopaminergic Markers. *J. Neurosci. Res.* **1993**, *35*, 67−82.

(10) Sengstock, G. J.; Olanow, C. W.; Dunn, A. J.; Barone, S., Jr.; Arendash, G. W. Progressive Changes in Striatal Dopaminergic Markers, Nigral Volume, and Rotational Behavior Following Iron Infusion into the Rat Substantia Nigra. *Exp. Neurol.* **1994**, *130*, 82−94.

(11) Jiang, H.; Song, N.; Wang, J.; Ren, L. Y.; Xie, J. X. Peripheral Iron Dextran Induced Degeneration of Dopaminergic Neurons in Rat Substantia Nigra. *Neurochem. Int.* **2007**, *51*, 32−36.

(12) Bayanzay, K.; Alzoebie, L. Reducing the Iron Burden and Improving Survival in Transfusion-Dependent Thalassemia Patients: Current Perspectives. *J. Blood Med.* **2016**, *7*, 159−169.

(13) Shah, J.; Kurtin, S. E.; Arnold, L.; Lindroos-Kolqvist, P.; Tinsley, S. Management of Transfusion-Related Iron Overload in Patients with Myelodysplastic Syndromes. *Clin J. Oncol Nurs* **2012**, *16*, 37−46.

(14) Guo, C.; Hao, L. J.; Yang, Z. H.; Chai, R.; Zhang, S.; Gu, Y.; Gao, H. L.; Zhong, M. L.; Wang, T.; Li, J. Y.; Wang, Z. Y. Deferoxamine-Mediated Up-Regulation of HIF-1alpha Prevents Dopaminergic Neuronal Death *via* the Activation of MAPK Family Proteins in MPTP-Treated Mice. *Exp. Neurol.* **2016**, *280*, 13−23.

(15) Aguirre, P.; Mena, N. P.; Carrasco, C. M.; Munoz, Y.; Perez-Henriquez, P.; Morales, R. A.; Cassels, B. K.; Mendez-Galvez, C.; Garcia-Beltran, O.; Gonzalez-Billault, C.; Nunez, M. T. Iron Chelators and Antioxidants Regenerate Neuritic Tree and Nigrostriatal Fibers of MPP+/MPTP-Lesioned Dopaminergic Neurons. *PLoS One* **2015**, *10*, e0144848.

(16) May, P. M.; Bulman, R. A. The Present Status of Chelating Agents in Medicine. *Prog. Med. Chem.* **1983**, *20*, 225−336.

(17) Olivieri, N. F.; Brittenham, G. M. Iron-Chelating Therapy and the Treatment of Thalassemia. *Blood* **1997**, *89*, 739−761.

(18) Richardson, D. R.; Ponka, P. Development of Iron Chelators to Treat Iron Overload Disease and Their Use as Experimental Tools to Probe Intracellular Iron Metabolism. *Am. J. Hematol.* **1998**, *58*, 299−305.

(19) Lynch, S. G.; Fonseca, T.; LeVine, S. M. A Multiple Course Trial of Desferrioxamine in Chronic Progressive Multiple Sclerosis. *Cell Mol. Biol. (Noisy-le-grand)* **2000**, *46*, 865−869.

(20) Pahuja, R.; Seth, K.; Shukla, A.; Shukla, R. K.; Bhatnagar, P.; Chauhan, L. K. S.; Saxena, P. N.; Arun, J.; Chaudhari, B. P.; Patel, D. K.; Singh, S. P.; Shukla, R.; Khanna, V. K.; Kumar, P.; Chaturvedi, R. K.; Gupta, K. C. Trans-Blood Brain Barrier Delivery of Dopamine-Loaded Nanoparticles Reverses Functional Deficits in Parkinsonian Rats. *ACS Nano* **2015**, *9*, 4850−4871.

(21) Kozlu, S.; Caban, S.; Yerlikaya, F.; Fernandez-Megia, E.; Novoa-Carballal, R.; Riguera, R.; Yemisci, M.; Gursoy-Ozdemir, Y.; Dalkara, T.; Couvreur, P.; Capan, Y. An Aquaporin 4 Antisense Oligonucleotide Loaded, Brain Targeted Nanoparticulate System Design. *Pharmazie* **2014**, *69*, 340−345.

(22) Lentz, T. L.; Burrage, T. G.; Smith, A. L.; Crick, J.; Tignor, G. H. Is the Acetylcholine-Receptor a Rabies Virus Receptor. *Science* **1982**, *215*, 182−184.

(23) Kim, J. Y.; Choi, W. I.; Kim, Y. H.; Tae, G. Brain-Targeted Delivery of Protein Using Chitosan- and RVG Peptide-Conjugated, Pluronic-Based Nano-Carrier. *Biomaterials* **2013**, *34*, 1170−1178.

(24) Liu, Y.; Guo, Y.; An, S.; Kuang, Y.; He, X.; Ma, H.; Li, J.; Lv, J.; Zhang, N.; Jiang, C. Targeting Caspase-3 as Dual Therapeutic Benefits by RNAi Facilitating Brain-Targeted Nanoparticles in a Rat Model of Parkinson's Disease. *PLoS One* **2013**, *8*, e62905.

(25) Lafon, M. Rabies Virus Receptors. *J. NeuroVirol.* **2005**, *11*, 82−87.

(26) Liu, Y.; Huang, R. Q.; Han, L.; Ke, W. L.; Shao, K.; Ye, L. Y.; Lou, J. N.; Jiang, C. Brain-Targeting Gene Delivery and Cellular Internalization Mechanisms for Modified Rabies Virus Glycoprotein RVG29 Nanoparticles. *Biomaterials* **2009**, *30*, 4195−4202.

(27) Gong, C.; Li, X. N.; Xu, L. L.; Zhang, Y. H. Target Delivery of a Gene into the Brain Using the RVG29-Oligoarginine Peptide. *Biomaterials* **2012**, *33*, 3456−3463.

(28) Yang, Y. J.; Zhao, P. S.; Wu, H. X.; Wang, H. L.; Zhao, L. L.; Xue, X. H.; Gai, W. W.; Gao, Y. W.; Yang, S. T.; Xia, X. Z. Production and Characterization of a Fusion Peptide Derived from the Rabies Virus Glycoprotein (RVG29). *Protein Expression Purif.* **2014**, *104*, 7−13.

(29) Wang, H.; Wu, Y.; Zhao, R.; Nie, G. Engineering the Assemblies of Biomaterial Nanocarriers for Delivery of Multiple Theranostic Agents with Enhanced Antitumor Efficacy. *Adv. Mater.* **2013**, *25*, 1616−1622.

(30) Zhao, X.; Li, F.; Li, Y.; Wang, H.; Ren, H.; Chen, J.; Nie, G.; Hao, J. Co-Delivery of HIF1alpha siRNA and Gemcitabine *via* Biocompatible Lipid-Polymer Hybrid Nanoparticles for Effective Treatment of Pancreatic Cancer. *Biomaterials* **2015**, *46*, 13−25.

DOI: 10.1021/acsnano.7b08172
ACS Nano XXXX, XXX, XXX−XXX

(31) Le Roy, C.; Wrana, J. L. Clathrin- and Non-Clathrin-Mediated Endocytic Regulation of Cell Signalling. Nature reviews. *Nat. Rev. Mol. Cell Biol.* **2005**, *6*, 112−126.
(32) Tahara, K.; Sakai, T.; Yamamoto, H.; Takeuchi, H.; Hirashima, N.; Kawashima, Y. Improved Cellular Uptake of Chitosan-Modified PLGA Nanospheres by A549 Cells. *Int. J. Pharm.* **2009**, *382*, 198−204.
(33) Hillaireau, H.; Couvreur, P. Nanocarriers' Entry into the Cell: Relevance to Drug Delivery. *Cell. Mol. Life Sci.* **2009**, *66*, 2873−2896.
(34) Barros, D.; Costa Lima, S. A.; Cordeiro-da-Silva, A. Surface Functionalization of Polymeric Nanospheres Modulates Macrophage Activation: Relevance in Leishmaniasis Therapy. *Nanomedicine* **2015**, *10*, 387−403.
(35) Neves, A. R.; Queiroz, J. F.; Lima, S. A. C.; Reis, S. Apo E-Functionalization of Solid Lipid Nanoparticles Enhances Brain Drug Delivery: Uptake Mechanism and Transport Pathways. *Bioconjugate Chem.* **2017**, *28*, 995−1004.
(36) Chai, G. H.; Hu, F. Q.; Sun, J. H.; Du, Y. Z.; You, J.; Yuan, H. Transport Pathways of Solid Lipid Nanoparticles Across Madin-Darby Canine Kidney Epithelial Cell Monolayer. *Mol. Pharmaceutics* **2014**, *11*, 3716−3726.
(37) Conner, S. D.; Schmid, S. L. Regulated Portals of Entry into the Cell. *Nature* **2003**, *422*, 37−44.
(38) Petros, R. A.; DeSimone, J. M. Strategies in the Design of Nanoparticles for Therapeutic Applications. *Nat. Rev. Drug Discovery* **2010**, *9*, 615−627.
(39) Ashfaq, U. A.; Javed, T.; Rehman, S.; Nawaz, Z.; Riazuddin, S. Lysosomotropic Agents as HCV Entry Inhibitors. *Virol. J.* **2011**, *8*, 163.
(40) Xie, Y.; Ye, L. Y.; Zhang, X. B.; Hou, X. P.; Lou, J. N. Establishment of an *in Vitro* Model of Brain-Blood Barrier. *Health Sciences* **2004**, *36*, 435−438.
(41) Kumar, P.; Wu, H.; McBride, J. L.; Jung, K. E.; Kim, M. H.; Davidson, B. L.; Lee, S. K.; Shankar, P.; Manjunath, N. Transvascular Delivery of Small Interfering RNA to the Central Nervous System. *Nature* **2007**, *448*, 39−43.
(42) Tiwari, M. N.; Agarwal, S.; Bhatnagar, P.; Singhal, N. K.; Tiwari, S. K.; Kumar, P.; Chauhan, L. K.; Patel, D. K.; Chaturvedi, R. K.; Singh, M. P.; Gupta, K. C. Nicotine-Encapsulated Poly(lactic-co-glycolic) Acid Nanoparticles Improve Neuroprotective Efficacy against MPTP-Induced Parkinsonism. *Free Radical Biol. Med.* **2013**, *65*, 704−718.
(43) Chaturvedi, R. K.; Shukla, S.; Seth, K.; Agrawal, A. K. Zuckerkandl's Organ Improves Long-Term Survival and Function of Neural Stem Cell Derived Dopaminergic Neurons in Parkinsonian Rats. *Exp. Neurol.* **2008**, *210*, 608−623.
(44) Bonini, N. M.; Giasson, B. I. Snaring the Function of Alpha-Synuclein. *Cell* **2005**, *123*, 359−361.
(45) Uversky, V. N. Neuropathology, Biochemistry, and Biophysics of Alpha-Synuclein Aggregation. *J. Neurochem.* **2007**, *103*, 17−37.
(46) Kostka, M.; Hogen, T.; Danzer, K. M.; Levin, J.; Habeck, M.; Wirth, A.; Wagner, R.; Glabe, C. G.; Finger, S.; Heinzelmann, U.; Garidel, P.; Duan, W.; Ross, C. A.; Kretzschmar, H.; Giese, A. Single Particle Characterization of Iron-Induced Pore-Forming Alpha-Synuclein Oligomers. *J. Biol. Chem.* **2008**, *283*, 10992−1003.
(47) Olivier, J. C.; Huertas, R.; Lee, H. J.; Calon, F.; Pardridge, W. M. Synthesis of Pegylated Immunonanoparticles. *Pharm. Res.* **2002**, *19*, 1137−1143.
(48) Wan, W. B.; Cao, L.; Liu, L. M.; Kalionis, B.; Chen, C.; Tai, X. T.; Li, Y. M.; Xia, S. J. EGb761 Provides a Protective Effect against Abeta1−42 Oligomer-Induced Cell Damage and Blood-Brain Barrier Disruption in an *in Vitro* bEnd.3 Endothelial Model. *PLoS One* **2014**, *9*, e113126.
(49) Chen, Z.; Zhai, M.; Xie, X.; Zhang, Y.; Ma, S.; Li, Z.; Yu, F.; Zhao, B.; Zhang, M.; Yang, Y.; Mei, X. Apoferritin Nanocage for Brain Targeted Doxorubicin Delivery. *Mol. Pharmaceutics* **2017**, *14*, 3087−3097.
(50) Elbakry, A.; Zaky, A.; Liebl, R.; Rachel, R.; Goepferich, A.; Breunig, M. Layer-by-Layer Assembled Gold Nanoparticles for siRNA Delivery. *Nano Lett.* **2009**, *9*, 2059−2064.
(51) Song, Q.; Huang, M.; Yao, L.; Wang, X.; Gu, X.; Chen, J.; Huang, J.; Hu, Q.; Kang, T.; Rong, Z.; Qi, H.; Zheng, G.; Chen, H.; Gao, X. Lipoprotein-Based Nanoparticles Rescue the Memory Loss of Mice with Alzheimer's Disease by Accelerating the Clearance of Amyloid-Beta. *ACS Nano* **2014**, *8*, 2345−2359.
(52) Shao, W.; Zhang, S. Z.; Tang, M.; Zhang, X. H.; Zhou, Z.; Yin, Y. Q.; Zhou, Q. B.; Huang, Y. Y.; Liu, Y. J.; Wawrousek, E.; Chen, T.; Li, S. B.; Xu, M.; Zhou, J. N.; Hu, G.; Zhou, J. W. Suppression of Neuroinflammation by Astrocytic Dopamine D2 Receptors *via* AlphaB-Crystallin. *Nature* **2013**, *494*, 90−94.
(53) Guo, X. L.; Zheng, H.; Guo, Y. T.; Wang, Y.; Anderson, G. J.; Ci, Y. Z.; Yu, P.; Geng, L. N.; Chang, Y. Z. Nasal Delivery of Nanoliposome-Encapsulated Ferric Ammonium Citrate can Increase the Iron Content of Rat Brain. *J. Nanobiotechnol.* **2017**, *15*, 42.
(54) You, L. H.; Yan, C. Z.; Zheng, B. J.; Ci, Y. Z.; Chang, S. Y.; Yu, P.; Gao, G. F.; Li, H. Y.; Dong, T. Y.; Chang, Y. Z. Astrocyte Hepcidin is a Key Factor in LPS-Induced Neuronal Apoptosis. *Cell Death Dis.* **2017**, *8*, e2676.

DOI: 10.1021/acsnano.7b08172
ACS Nano XXXX, XXX, XXX−XXX